Nondegenerate Josephson Mixers with Enhanced Bandwidth and Saturation Power for Quantum Signal Amplification and Transduction

Baleegh Abdo, Dongbing Shao, Shayne Cairns, Jae-woong Nah, Oblesh Jinka, Srikanth Srinivasan, Thomas McConkey, Vincent Arena, and Corrado Mancini *IBM Quantum, IBM Research Center, Yorktown Heights, New York 10598, USA.*(Dated: August 12, 2025)

Nondegenerate Josephson mixers (JMs), formed by coupling two different transmission-line resonators to Josephson ring modulators (JRMs), are vital and versatile devices capable of processing microwave signals at the quantum limit. Owing to the lossless nondegenerate three-wave mixing process enabled by the JRM, JMs can perform phase preserving amplification of quantum signals, generate two-mode squeezed states, and perform noiseless frequency conversion. However, due to their limited bandwidth and saturation power, such resonator-based JMs are generally unable to simultaneously process frequency-multiplexed signals required in large quantum processors. To overcome this longstanding dual challenge, we redesign the JRM parameters by optimizing its inductances to suppress higher order mixing products and engineer its electromagnetic environment by incorporating lumped-element coupled-mode networks between the JRM and the two distinct ports of the JM. By implementing these strategies, we measure for JMs realized with four coupled modes per port, operated in amplification (conversion), bandwidths of about 400 MHz (700 MHz) with power reflections above 10 dB (below -10 dB) and saturation powers of about -110 dBm at 15 dB (-91 dBm at -26 dB). Similarly, we demonstrate for a low external quality factor resonant-mode JM operated in conversion, a maximum bandwidth of about 670 MHz with power reflections below -10 dB and a maximum saturation power of about −86 dBm at −17 dB. Such nondegenerate JMs with enhanced bandwidths and saturation powers could serve in a variety of frequency-multiplexed settings ranging from high fidelity qubit readout and unidirectional routing of quantum signals to generation of remote entanglement with continuous variables.

I. INTRODUCTION

Nonlinear Josephson-based devices capable of amplifying quantum microwave signals with minimum added noise set by quantum mechanics [1-3], play a pivotal role in the readout chains of superconducting quantum processors [4–6]. When used as first-stage amplifiers, employing three-wave or four-wave mixing processes, they remarkably enable real-time, high-fidelity, single-shot, QND readout of qubit states [7–10]. Moreover, since such nonlinear mixing devices can operate, under certain conditions, as noiseless frequency converters [11, 12], they could potentially play other crucial roles in large quantum processors. Such as transducing quantum states between different frequencies [13–15] or forming on-chip nonreciprocal devices that replace bulky off-chip magnetic isolators commonly utilized in the protection of qubits against noise coming down the output chain [16–22].

In recent years, two prominent and distinct platforms of low-loss and low-noise Josephson parametric devices have emerged. The first is resonator based. It embeds a Josephson nonlinear medium, such as dc-SQUIDs [23], SNAILs [24] or Josephson ring modulators (JRMs) [25, 26] into microwave resonators. JRM-based parametric devices are particularly advantageous owing to their nondegnerate nature, i.e., having two spectrally different modes with two separate physical ports [27, 28] and their three-wave mixing operation in which the pump tone frequency lies out of the device band and can be fed to it via a separate port [29]. The second is transmission-line based. It forms a semi-continuous nonlinear trans-

mission line made of an array of hundreds to thousands of Josephson elements, such as Josephson junctions [30–33], SNAILs [34, 35], and rf-SQUIDs [36, 37], that are capacitively coupled to ground and periodically interleaved in some designs with linear resonant circuits, primarily engineered to enable phase matching between the various traveling waves taking part in the mixing process [38].

Owing to these basic differences in the engineered electromagnetic environment, the two platforms of Josephson parametric devices exhibit different figures, in particular with respect to added noise, insertion loss, maximum gain or transmission, bandwidth, and saturation power. While the resonator-based devices generally exhibit better performance with regard to the first three metrics, they tend to have very narrow bandwidths and low saturation powers, which preclude them from being used in hardware-efficient, frequency-multiplexed schemes required in large quantum processors. In contrast, the transmission-line devices, due to their distributed nature, generally achieve broad bandwidths spanning a few gigahertz and large saturation powers exceeding -110 dBm, which make them indispensable in large quantum systems [30–32].

However, despite the practical utility and reliable performance of traveling-wave parametric devices (TWPAs), they possess a few disadvantages when deployed for qubit readout. While their broad bandwidth of $2-5~\mathrm{GHz}$ is generally considered a major advantage, it is also a liability since it requires for its proper operation well-matched 50 Ohm environment at its input and output ports over the same bandwidth and amplifies more noise

than necessary over its wide bandwidth, including the unwanted qubit frequency band, while most qubit readout signals reside in a much narrower band of about 1
GHz or less [39]. As a result, it is imperative to pair TWPAs with broadband isolators to provide sufficient broadband impedance matching and qubit protection against
reflected amplified signals or noise [30]. Another notable
disadvantage of typical TWPAs is the unintended generation and phase-matching of higher-order mixing products
[40], which result in reduction of the qubit measurement
efficiency and could cause instabilities if the device ports
are not well matched out of band as well.

One promising scheme to overcome some of these drawbacks applies impedance-matching techniques to resonator-based devices, which ideally boost their bandwidths without compromising their core strengths [41]. However, all experimental realizations to date achieve bandwidth enhancement in amplification and conversion via impedance matching of grounded Josephson elements, such as dc-SQUIDs and interleaved arrays of rf-SQUIDs. Furthermore, most experimental works apply impedance-matching to doubly degenerate parametric devices that have one physical port for the processed signal and one resonance mode [42–48].

In this work, we extend the impedance-matching design technique to nondegenerate Josephson mixers, that have two physical ports and two resonance modes and whose nonlinear medium, i.e., the JRM, has four main nodes, none of which can be shorted to ground. Furthermore, we incorporate into the new designs key theoretical and experimental lessons shown to enhance the saturation power of JMs [49, 50], such as designing them to operate as close as possible to Kerr-nulling working points of the JRM, and realizing favorable inductance ratios between the inductances of the JRMs and the resonators they are embedded into [51, 52].

Furthermore, we implement the new JM designs using a trilayer Nb process typically used in the fabrication of TWPAs [30] and SQUIDs [53], which enable us, among other things, to realize the required lumped-element capacitors and inductors. In particular, we realize and measure four JM devices of the new design and fabrication process. Two of them implement lumped-element resonator-based JMs, which we refer to as resonant-mode JMs, while the other two incorporate matching networks, which we refer to as coupled-mode JMs. We show that the redesigned lumped-element JM devices can operate near the quantum limit in amplification and frequency We demonstrate that a lumped-element, conversion. resonant-mode JM device with low external quality factor can achieve relatively large bandwidths and saturation powers, i.e., about 600 MHz and above -100 dBm, when operated in conversion mode, which, unlike the amplification mode, does not follow the amplitude-gain bandwidth product, known to significantly limit the dynamical bandwidths of parametric amplifiers at high gains [26, 28]. Also, importantly, we show that the coupledmode JMs exhibit enhanced bandwidths and saturation

powers in amplification (conversion) of about 400 MHz (700 MHz) and -110 dBm (-95 dBm).

II. THREE-WAVE MIXING WITH THE JRM

An ideal nondegenerate three-wave mixing device absorbs three input signals, referred to as signal, idler, and pump with distinct angular frequencies ω_s , ω_i , and ω_p , and complex amplitudes $A_s^{\rm in}$, $A_i^{\rm in}$, and $A_p^{\rm in}$, where ω_p corresponds to either the frequency sum $\omega_s + \omega_i$ or difference $|\omega_i - \omega_s|$ and emits output signals at the same frequencies with amplitudes $A_s^{\rm out}$, $A_i^{\rm out}$, and $A_p^{\rm out}$, which, without internal dissipation, satisfy the energy conservation condition $|A_s^{\rm in}|^2 + |A_i^{\rm in}|^2 + |A_p^{\rm in}|^2 = |A_s^{\rm out}|^2 + |A_i^{\rm out}|^2 + |A_p^{\rm out}|^2$. When a strong coherent pump tone is applied, i.e.,

When a strong coherent pump tone is applied, i.e., $\left|A_p^{\rm in}\right|^2\gg\left|A_s^{\rm in}\right|^2$, $\left|A_i^{\rm in}\right|^2$ such a device can operate in two modes depending on the pump frequency, (1) signal and idler amplification with photon gain when $\omega_p=\omega_s+\omega_i$, and (2) noiseless frequency conversion without photon gain between the signal and idler when $\omega_p=|\omega_i-\omega_i|$. While in the former case, the pump drive, which undergoes a downconversion process, supplies the extra photon numbers in the emitted signals, in the latter case, the pump drive provides the energy difference between the photons at ω_i and ω_s .

The JRM, which is the nonlinear element in nondegenerate JM devices, implements such dispersive three-wave mixing operation in the microwave domain. It consists of four Josephson junctions, each with Josephson inductance $L_{J0} = \varphi_0/I_0$, forming a small superconducting loop, i.e., $L_{J0} \gg L_s$, which is threaded by an external flux Φ_e and has the symmetry of a Wheatstone bridge as shown in Fig. 1(a). Due to the JRM structure and symmetry, its four nodes couple to three orthogonal spatial modes, two that are differential φ_a and φ_b corresponding to the signal and idler, while the third φ_c is a common excitation corresponding to the pump. Expressing the normal modes φ_a , φ_b , φ_c in terms of the dimensionless node fluxes φ_1 , φ_2 , φ_3 , φ_4 (shown in Fig. 1 (a)) gives $\varphi_a = \varphi_1 - \varphi_3$, $\varphi_b = \varphi_2 - \varphi_4$, and $\varphi_c = \varphi_1 + \varphi_3 - \varphi_2 - \varphi_4$, where $\varphi_j(t) = \frac{1}{\varphi_0} \int_{-\infty}^t V(t') dt'$ for node j and $\varphi_0 = \hbar/2e$ is the reduced flux quantum.

Using the normal spatial modes, the energy of the JRM can be written as [52]

$$E_{\text{JRM}} = -4E_J \cos\left(\frac{\varphi_a}{2}\right) \cos\left(\frac{\varphi_b}{2}\right) \cos\left(\frac{\varphi_c}{2}\right) \cos\left(\frac{\varphi_e}{4}\right) -4E_J \sin\left(\frac{\varphi_a}{2}\right) \sin\left(\frac{\varphi_b}{2}\right) \sin\left(\frac{\varphi_c}{2}\right) \sin\left(\frac{\varphi_e}{4}\right) +\frac{E_L}{4} \left(\varphi_a^2 + \varphi_b^2 + \frac{\varphi_c^2}{2}\right),$$
 (1)

where $E_J = \varphi_0 I_0$ is the Josephson energy, $E_L = \varphi_0^2 / L_{in}$ is the energy associated with each of the linear inductors L_{in} inside the loop, and $\varphi_e = \Phi_e / \varphi_0$.

Expanding E_{JRM} around the ground state, i.e., $\varphi_a = \varphi_b = \varphi_c = 0$, which we assume is stable as we vary the external flux bias, we get [51]

$$\begin{split} E_{\text{JRM}} &= -\frac{1}{2} E_J \sin\left(\frac{\varphi_e}{4}\right) \varphi_a \varphi_b \varphi_c \\ &+ \left[\frac{E_L}{4} + \frac{E_J}{2} \cos\left(\frac{\varphi_e}{4}\right)\right] \left(\varphi_a^2 + \varphi_b^2\right) \\ &+ \left[\frac{E_L}{8} + \frac{E_J}{2} \cos\left(\frac{\varphi_e}{4}\right)\right] \varphi_c^2 + O\left(\varphi_{a,b,c}^4\right). \end{split} \tag{2}$$

The first term in Eq. (2) is the trilinear coupling term that gives rise to the desired three-wave mixing operation, whereas all the other couplings can be detrimental to the ideal performance of the device. As seen in Eq. (1), the nonlinear couplings are controlled by the external magnetic flux φ_e . The Kerr nulling point for which the even-order couplings set by the cosine terms in Eq. (1) vanish, is attained at $\varphi_e = 2\pi$ (corresponding to $\Phi_e = \Phi_0$, where Φ_0 is the flux quantum).

Furthermore, using the series expansion of the dimensionless potential energy $E'_{JRM} = E_{JRM}/E_L$, we obtain the dimensionless unpumped three-mode coupling strength

$$g = \frac{1}{2\beta} \sin\left(\frac{\varphi_e}{4}\right),\tag{3}$$

where the inductance ratio $\beta = L_{J0}/L_{in}$ sets the overall strength of the nonlinearity.

Another design parameter that significantly influences the strength of the various coupling terms of the mixing process is the participation ratio 0 , which represents the fraction of the mode power within the JM device that is carried by the JRM [28, 52, 54].

Generally, lowering p, e.g., by increasing the series inductance outside the ring L_{out} , decreases the JRM nonlinearity by suppressing all coupling terms, but the suppression is not uniform. The higher order coupling terms get reduced more than the lower order ones. Thus, in certain parameter space, primarily of β and p investigated in Ref. [52], decreasing p can boost the JM saturation power.

III. THE DEVICE CIRCUIT

The circuit elements of the realized JMs are shown in Fig. 1 (a). At the center, lies the JRM, which consists of four nominally identical Nb Josephson junctions connected in a superconducting loop. Each pair of opposite nodes is connected to linear outer inductors L_{out} and shunted by plate capacitors C_a and C_b , which together with the JRM inductance set the bare differential mode resonance frequencies for mode a and b. L_s represents the geometric (stray) inductance associated with

the superconducting leads connecting adjacent Josephson junctions. Inside the loop, the JRM junctions are shunted by linear inductors, i.e., L_{in} , which play two key roles, (1) they eliminate the hysteretic dependence of the JRM on the external flux threading the loop Φ_e [51], thus making the bare resonance frequencies of the device tunable with flux. Such flux-tunability is highly desirable and particularly crucial when frequency matching is required between various quantum devices [9], (2) they set the parameter β , which determines, as seen in Eq. (3), the coupling parameter g of the wave-mixing process that affects, among other figures, the saturation power of the JM and the maximum achievable gain in amplification or transmission in conversion.

The blocks marked as M_a as M_b , refer to impedance-matching networks, which connect the electrodes of the shunt capacitors C_a and C_b to the corresponding external ports of mode a and mode b, i.e., $A_{1,2}$ and $B_{1,2}$. In Fig. 1 (b) and (c) we depict the two circuit configurations for the M_k blocks employed in this work, where the index k refers to mode a or b. The configuration of panel (b), applicable to JM_1 and JM_2 devices (see Table I), realizes direct leads (transmission lines) between node J_i and port K_i . Whereas, the configuration of panel (c), applicable to JM_3 and JM_4 (see Table I), realizes three alternating coupling capacitors and LC resonators shorted to ground between ports J_i and K_i .

The pump drive is fed to the JM through a separate port P connected to an on-chip transmission line as shown in panel (a). The pump transmission line is capacitively coupled via small plate capacitors $C_{cp} \simeq 60$ fF to the electrodes of the shunt capacitors C_a and C_b , which are connected via L_{out} to the four nodes of the JRM. To ensure that the pump drive excites the common mode of the JRM, i.e., opposite nodes are driven by the same polarity, we separate the coupling points to C_a and C_b by an on-chip transmission line of length $\lambda_p/2$, corresponding to a π phase shift, where λ_p refers to the mean pump wavelength. Furthermore, to ensure having rf-voltage anti-nodes near the locations of C_{cp} , we add a $\lambda_p/4$ section shorted to ground after the last C_{cp} .

In Fig. 1 (d), we exhibit an optical image of a JM₂ chip, which features the capacitively shunted JRM at the center, the bump-bonding sites (black circles), and the launching pads for ports $A_{1,2}$, $B_{1,2}$, and P on the periphery. A zoom-in image of the device center is shown in Fig. 1 (e). It displays the JRM, the shunt capacitors $C_{a,b}$, the pump transmission line surrounding $C_{a,b}$, and the pump coupling capacitors C_{cp} . A further zoom-in on the JRM is exhibited in Fig. 1 (f). The layout featured in the image is applicable to JM_1 and JM_2 devices. Superconducting vias are used to connect two of the outer inductors to the electrodes of $C_{a,b}$, and connect the four L_{in} inside the JRM. A wire cross-over is formed between the bottom and left L_{out} , which are implemented using two different superconducting layers separated by an insulator. We estimate the parasitic capacitance introduced by the cross-over (which we neglect in our modeling) to

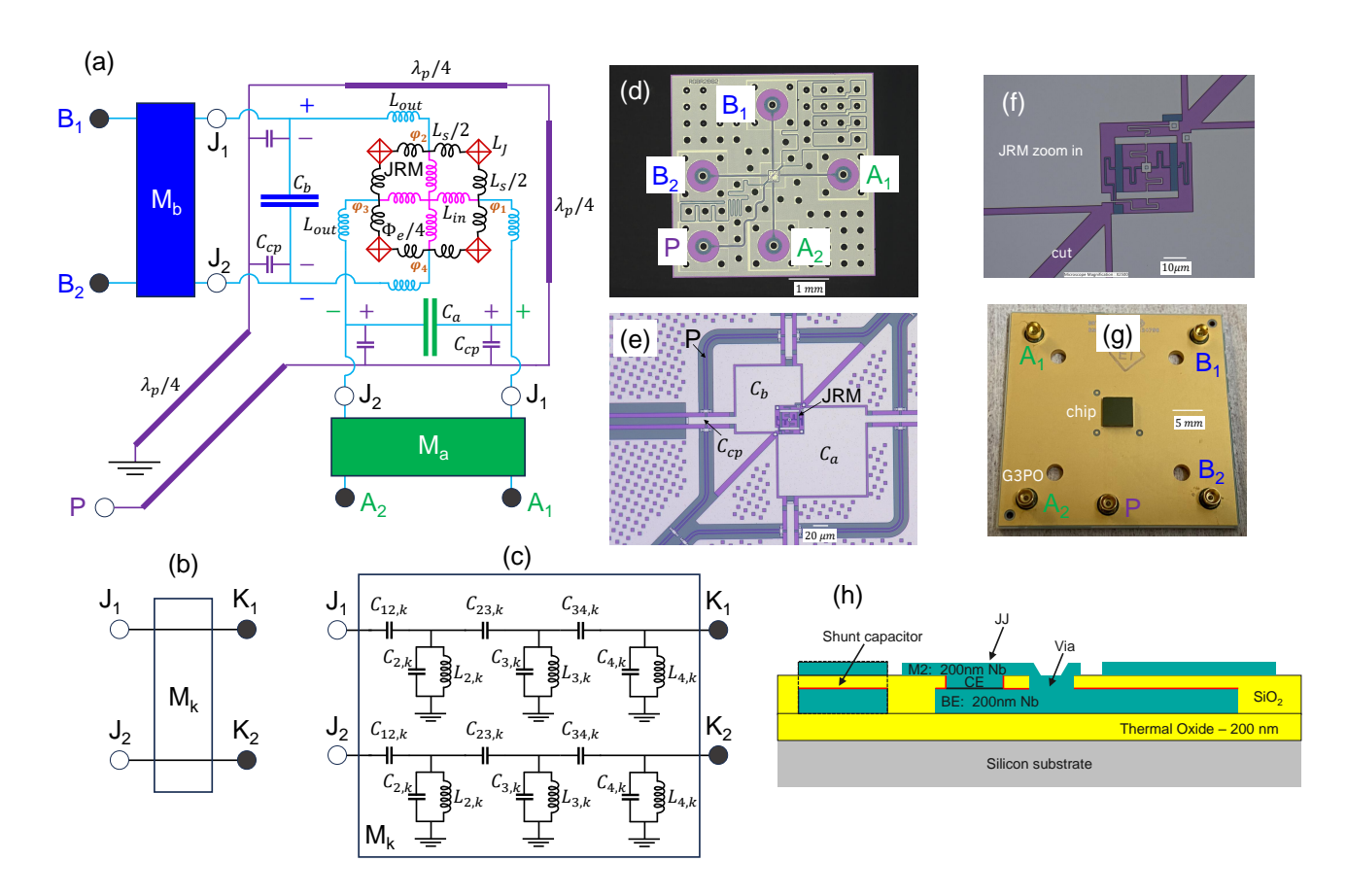


FIG. 1. (a) Circuit diagram of the impedance-matched, lumped-element Josephson mixers. The capacitively-shunted JRM is connected to the device ports $A_{1,2}$ and $B_{1,2}$ through direct transmission lines for JM₁ and JM₂ as illustrated in (b), or through capacitively coupled three LC resonators for JM₃ and JM₄ as shown in (c). (d) Optical image of a JM₂ chip. The black disks on chip represent bump bonding sites. The launch pads for ports A, B, and P are located on the periphery. (e) Optical image of the capacitively shunted JRM. (f) A zoom-in on the JRM configuration incorporated in JM₁ and JM₂. (g) Image of a bump-bonded JM to a PCB and the G3PO connectors used for delivering the input and output signals. (h) Diagram of the multi-layer stack that implements three key elements of the JMs namely, plate capacitors, Nb Josephson junctions, and vias. In the diagram, M2 represents the second layer of Nb, BE and CE correspond to the bottom and counter electrodes of the Josephson junctions, which are separated by a thin layer of Al/AlO_x (represented by the black line), whereas the thin red line represents an anodized NbO_x layer.

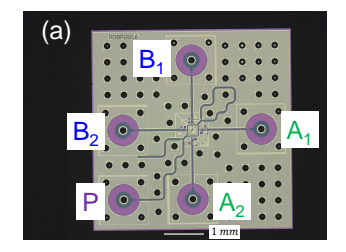
Device	JM_1	JM_2	JM_3	$ m JM_4$
Operation	Amplifier	Transducer	Amplifier	Transducer
Mode design	Resonant	Resonant	Coupled	Coupled
Modes per port	1	1	4	4

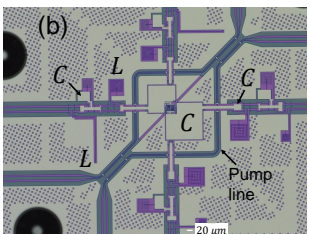
TABLE I. The operation and configuration of the JM devices presented in this work.

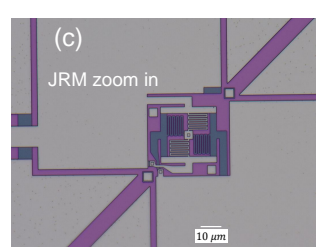
be small of about 0.13 fF (0.5 fF) in the case of $\rm JM_{1,2}$ ($\rm JM_{3,4}$). The design also includes a diagonal cut in the superconducting ground surrounding the JRM to suppress screening currents and thereby enable flux biasing of the JRM via a small superconducting coil mounted on top of the device cover. A photo of the JM chip bump bonded to a printed circuit board (PCB) with soldered G3PO connectors is shown in Fig.1 (g). A diagram of the multi-layer stack used in the fabrication of key ele-

ments of the JMs, such as Nb Josephson junctions, plate capacitors, and vias, is shown in Fig. 1 (h).

In Fig. 2, we exhibit additional four optical images, showing JM_3 and JM_4 devices. Panel (a) exhibits a photo of a JM_3 chip. Note that the on-chip pump line is much shorter in this instance than in Fig. 1 (d), since JM_3 is designed and operated as an amplifier, which requires significantly shorter pump wavelengths corresponding to higher pump frequencies than JM_2 operated as a freq-







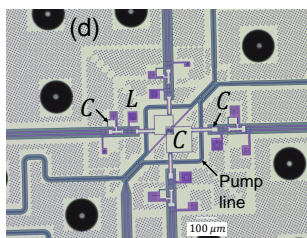


FIG. 2. (a) Photo of a JM₃ chip. (b) Zoom-in photo of a JM₃ chip, showing the capacitively-shunted JRM at the center and the capacitively-coupled LC resonators, which realize the lumped-element matching networks exhibited in Fig. 1 (c). (c) Optical image of the JRM incorporated in JM₃ and JM₄. (d) A similar image as (b) taken for a JM₄ chip.

uency converter (e.g., 18 GHz vs. 3 GHz). Photos of JM_3 and JM_4 chips featuring their capacitively-shunted JRMs and capacitively-coupled LC resonators are shown in (b) and (d), respectively. In these designs, plate capacitors are scaled based on their area, small inductors are realized as straight lines, while relatively large ones are realized as spirals.

A photo of the JRM employed in the design of JM₃ and JM₄ devices is shown in Fig. 2 (c). The JRM configuration in this case differs from the one incorporated in JM₁ and JM₂ (shown in Fig. 1 (f)) in three main aspects: (1) the critical current of the Josephson junctions is smaller, i.e., 2.5 μ A vs. 8.1 μ A, (2) L_{in} is larger, i.e., 30 pH vs. 11.3 pH, and (3) L_{out} is smaller, i.e., 9 pH vs. 27 pH (see Tables II, IV, V).

To model and design JMs, it is important to recognize the functional role played by the JRM. When driven by a pump tone at the frequency sum or difference between the nondegenerate idler (b) and signal (a) circuits connected to it, it acts as a parametric coupler mediating between them. At the circuit level, the nonlinear coupling introduced by the JRM can be modeled as a modulated mutual inductance as shown in Fig. 3 (a). In Fig. 3 (b), we present the equivalent two-port circuit model of the parametrically modulated mutual in the shunt representation corresponding to the amplification $(f_p = f_b + f_a)$ and transduction $(f_p = |f_b - f_a|)$ modes of operation, shown on the left- and right-hand side, respectively. One key advantage of employing JRMs to realize such parametric coupling over grounded SQUIDs for example is that with the former the coupling is purely parametric since it nulls the passive part of the coupling, i.e., $M_0 = 0$ (which is independent of the pump), thus providing same-frequency isolation between the signal and idler circuits.

IV. RESONANT-MODE JOSEPHSON MIXERS

In this section, we present measurements taken for the resonant-mode JM design, i.e., JM_1 and JM_2 . Both JM_1 and JM_2 devices share the same design, layout, and fabrication process. The main difference between them is in their mode of operation as listed in Table I, which leads

to different on-chip pump lines, especially with respect to their total length, set by the pump frequency range applicable in each case. Images of the pump lines employed in JM_1 and JM_2 devices can be seen in Fig. 2 (a) (belonging to JM_3) and Fig. 1 (d), respectively.

Based on the extracted design parameters of JM₁ and JM₂ (listed in Table II), we obtain $\beta \simeq 3.6$ and $p \simeq 0.58$, where p is evaluated using Eq. (B2). Moreover, since these JM devices consist of lumped-element parallel LC resonators directly connected to the external feedlines of impedance $Z_0 = 50$ Ohm, their total quality factors are dominated by their external quality factors given by $Q_a = Z_0/Z_a \cong 14.8$ and $Q_b = Z_0/Z_b \cong 10.6$, where $Z_a = \sqrt{L_a/C_a} \cong 3.4$ Ohm, and $Z_b = \sqrt{L_b/C_b} \cong 4.7$ Ohm (calculated for $\varphi_e = 0$). Using these calculated values, we find that despite having low external quality factors both JM₁ and JM₂ devices satisfy the stability condition, known as the pQ product, since $p^2Q_aQ_b \cong 53 \gg 1$ [26–28].

In Fig. 4 we exhibit several key measurements of JM₁. Plots (a) and (b), show reflection gain results S_{aa} and S_{bb} versus frequency measured for different working points, i.e., flux and pump parameters. The gain curves are normalized by the pump off response. Gain curves plotted with the same color in (a) and (b) are measured at the same working point. The measurement demonstrates that gains of 20 dB or more can be obtained for modes a and b over a tunable bandwidth of about 1.1 GHz and 600 MHz, respectively. In (c) and (d) we plot in using blue color one of the pump-on working points shown in (a) and (b) in yellow, which exhibit about 20 dB of gain and 30 MHz of bandwidth. We also plot for reference the pump-off data (black) and reflection calibration data (green) taken for the same setup and conditions but with open-end terminations replacing the JM devices (see experimental setup shown in Fig. 18). By comparing the pump off data to the reference curves, we observe insertion loss of 0.5 - 3.5 dB for mode a on resonance, and a negligible amount for mode b. Such a loss likely originates from dielectric loss in the plate capacitors.

In plot (e) and (f), we exhibit saturation power measurements taken on resonance at the same working point as (c) and (d). In these measurements, we fix the

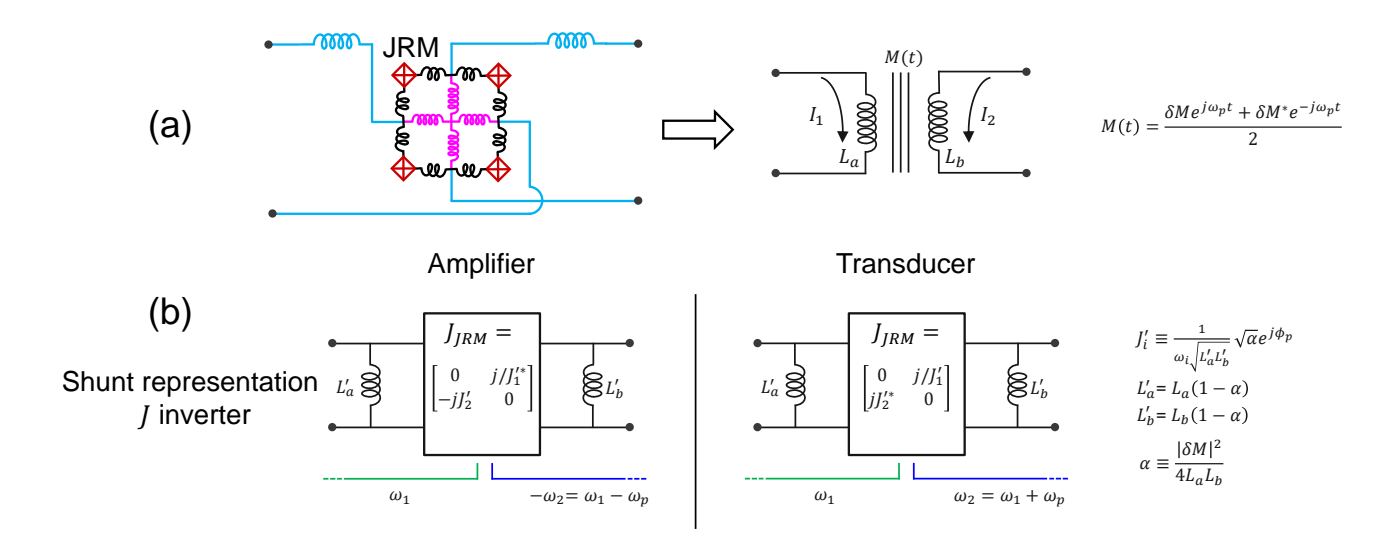


FIG. 3. (a) When driven by a pump, the JRM operation can be modeled as parametric-modulation of a mutual inductance M(t) between two linear inductors L_a and L_b with signal and idler currents I_1 and I_2 . (b) Equivalent two-port circuit model of the modulated mutual in the shunt representation corresponding to the amplification (left) and transduction (right) modes of operation. The boxed elements represent admittance inverters with the corresponding ABCD matrices J_{JRM} .

pump parameters to yield gains of about 20 dB (at sufficiently low signal power) and vary the input signal power applied to the JM at a certain frequency within its bandwidth. Saturation power indicated by red circles, i.e., -133 dBm in (e) and -132 dBm in (f), correspond to the minimum input power for which the gain changes by ± 1 dB relative to the low input power value.

To show that JM_1 amplifies near the quantum limit, we measure the SNR improvement of the output chain G/G_N versus the JM gain on resonance for modes a and b shown in subplots (g) and (h), respectively. By using Eq. (H2) to fit the data (black curve) we obtain estimates for T_N and $n_{\rm add}$, listed in the plot, which correspond to the effective noise temperature of the output chain and the noise-equivalent input photon number added by the JM.

Similar to subplots (c) and (d), panels (i) and (j), exhibit data taken for another working point originally shown in (a) and (b) in red, which exhibit maximum gains of about 26 dB and bandwidths of about 58 MHz at 20 dB. The pump-on gain curves (blue) are shown alongside the pump-off response (black) and the calibration reference (green). Like (c), the pump off response of the JM exhibits 1-3.5 dB of loss on resonance relative to the reference level.

As seen in Fig. 4, the measured gain curves generally have Lorentzian-like shapes and follow the amplitude-gain bandwidth product, which can be expressed as $\sqrt{G}B = \gamma$, where B is the dynamical bandwidth of the JM, $\gamma = 2\gamma_a\gamma_b/(\gamma_a\gamma_b)$ is the effective linear bandwidth of the JM, while γ_a and γ_b are the linear bandwidths of mode a and b, respectively. Based on the measured bandwidths $\gamma_a/2\pi \cong 400$ MHz and $\gamma_b \cong 1$ GHz for the

device, we get $B/2\pi \simeq 57$ MHz at power gain of 20 dB (i.e., G = 100), which is close to the measured values in Figs. 4(c),(d),(i),(j).

Using the transfer matrix model of the JM described in Appendix A and B and the device parameters listed in Table II (extracted from the fits to the resonance frequency data versus flux, depicted in Fig. 14 (a),(b)), we plot in panels (k) and (l) the calculated gain curves versus frequency of modes a and b which use the ideal lumped-element circuit of Fig. 1 (a), (b).

Similar to the measurements of (e) and (f), (m) and (n) exhibit saturation power measurement results for mode a and b taken on resonance at the working point of (i) and (i), which yield comparable saturation powers to (e) and (f), though obtained for about 3 dB higher power gains than (e) and (f). It is worth noting that in both cases (e),(f) and (m),(n), the saturation power measurement results exhibit a "shark-fin" feature, characterized by an initial rise in the gain with the input power followed by a monotonic decline. As shown in Refs. [49, 52], such a feature can be caused due to intrinsic self-Kerr or cross-Kerr effects (fourth-order coupling terms) that are dominant at the applied working point, or due to effective Kerr nonlinearity generated by a soft pump with only third-order couplings [52]. While the latter can be caused when the pump drive is partially in resonance with the device, the former can arise for example when operating away from the Kerr-nulling point, which, importantly, does not null both self-Kerr and cross-Kerr terms simultaneously when p < 1 [52].

Furthermore, similar to the calculated gain response of JM_1 presented in (k) and (l), we plot a microwave simulation result of S_{aa} versus frequency in panel (p).

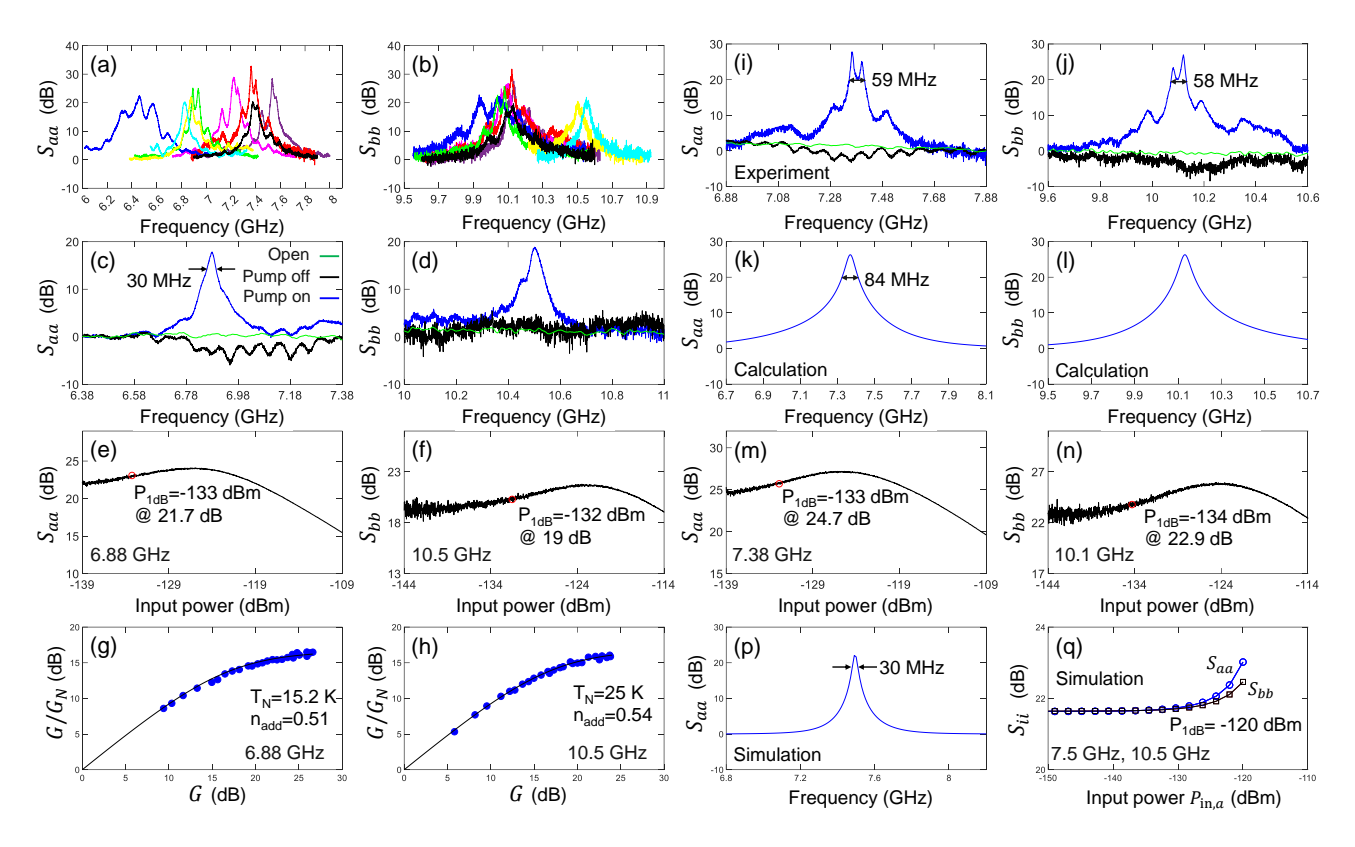


FIG. 4. (a) and (b) reflection gain measurement results S_{aa} and S_{bb} of JM₁ taken for different working points set by the applied flux, pump frequency, and power. Curves of the same color in (a) and (b) are taken at the same working point. (c) and (d) exhibit measured gain curves (blue) for one of the working points drawn in yellow in (a) and (b). The black curves correspond to the reflection parameters measured with pump off. The green curves, used as reference, are reflection parameters measured for open ends at nominally identical locations as the mounted devices. (e) and (f) saturation power measurements taken on resonance for the working point of (c) and (d). (g) and (h) SNR improvement for mode a and b measured versus the device gain (blue filled circles). The data is taken for the same flux and pump frequency as (c) and (d). The black curves represent theory fits. (i) and (j) same as (c) and (d) showing a different working point (red) exhibited in (a) and (b). (k) and (l) calculated response of the device that employs the extracted parameters listed in Table II. (m) and (n) saturation power measurements taken on resonance for the working point of (i) and (j). (p) Keysight ADS simulation of the reflection gain S_{aa} versus frequency. (q) Keysight ADS simulation of S_{aa} (blue circles) at 7.5 GHz and S_{bb} (black squares) at 10.5 GHz versus the signal power applied to port a.

The simulation is conducted using harmonic-balance in Keysight ADS (2023 version) based on the ideal lumpedelement model of the JM depicted in Fig. 1 (a),(b). In Fig. 4 (q), we plot the simulated results for S_{aa} and S_{bb} versus the input power applied to port a of the JM, i.e., $P_{\text{in},a}$, obtained on resonance at the same working point of panel (p). Further details regarding the simulation of JM devices are discussed in Appendix D.

While the simulation result yields a saturation power that is about 13 dB higher than in the experiment (-120 dBm vs. -133 dBm), the simulation result seems to capture the "shark-fin" feature exhibited by the data. In this context, it is important emphasize that the saturation power values strongly depend on the exact working point parameters, such as the flux bias, the pump frequency detuning relative to the sum of the resonance frequencies of mode a and b (which is more challenging to

determine in wideband devices), and the pump power. For instance, it has been shown in Ref. [49] that pump frequency detuning can influence the saturation power of a JM device by as much as 10 dB.

Another noteworthy working point of JM_1 , whose gain curves show pronounced deviation from the Lorentzain-like shape, is displayed in Fig. 5 (originally drawn in blue in Fig. 4 (a) and (b)). As seen in Fig. 5 (a) and (b), the measured gain curves S_{aa} and S_{bb} exhibit bandwidths of about 270 MHz and 307 MHz at 10 dB of gain, which are significantly larger than those obtained for the other working points presented in Fig. 4. For comparison, we plot in Fig. 5 (c) and (d), the calculated gain curves S_{aa} and S_{bb} versus frequency near the flux bias point applied in the experiment. Furthermore, as shown in Fig. 5 (e) and (f), the saturation powers achieved in this case, i.e., -115 dBm and -118 dBM, are at least 14 dB higher

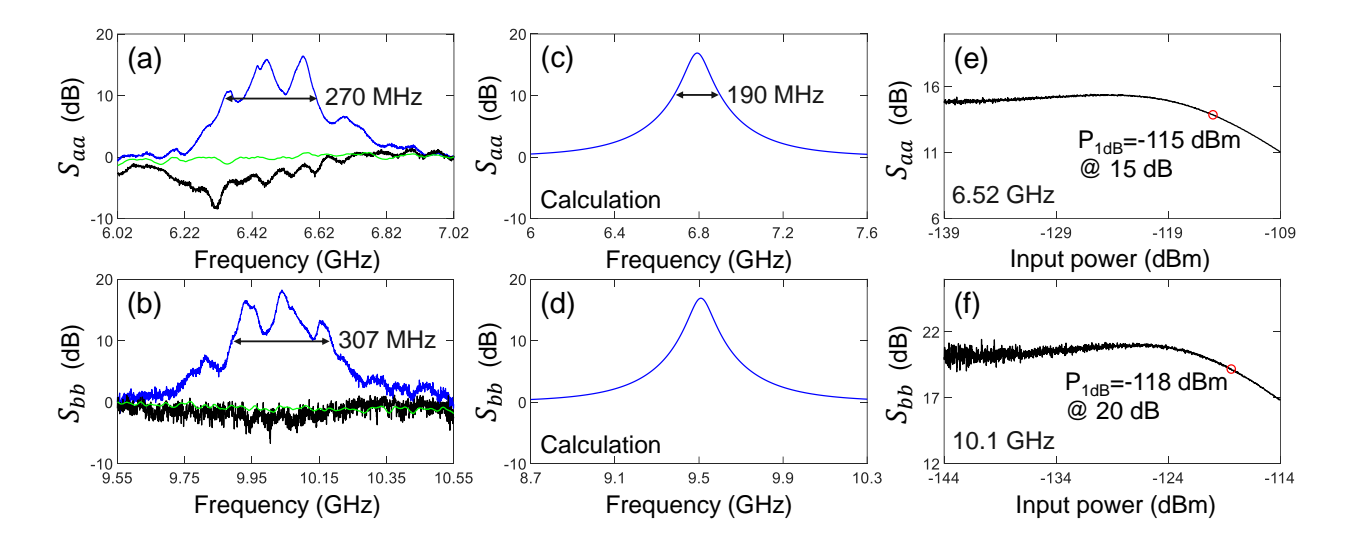


FIG. 5. (a) and (b) exhibit measured gain curves (blue) of another working point of JM₁ (shown in Fig. 4 (a) and (b) in blue). Similar to Fig. 4 (c) and (d) the black curves correspond to the reflection parameters measured with pump off and the green reference curves are reflection parameters measured for open ends at nominally identical locations as the mounted devices. The frequency range listed on the plots represent a bandwidth proxy taken at 10 dB. (c) and (d) Calculated response of JM₁ that employs the extracted parameters listed in Table II. (e) and (f) saturation power measurements taken at 6.52 GHz (S_{aa}) and 10.1 GHz (S_{bb}) for the working point of (a) and (b). Notably, the saturation powers obtained at this working point is about 14-19 dB higher than those measured in Fig. 4 (e), (f), (m), (n).

than what is measured for the other two working points in Fig. 4 of about -132 dBm.

One possible explanation for the significantly enhanced saturation power achieved in Fig. 5 compared to Fig. 4, is that the flux bias $\Phi_e = 1.6\Phi_0$ in the measurement of Fig. 5 is closer to a Kerr-nulling point for the device compared to $\Phi_e = 1.24\Phi_0$ in Fig. 4 (m),(n) (see Table VI). Such a deviation of the Kerr-nulling point from the $\Phi_e = \Phi_0$ value, can be explained by the presence of $L_s \neq 0$ in our device, which is known to shift the Kerr-nulling point upwards as L_s is increased. Moreover, based on a calculation in Ref. [50] (done for $\beta = 4.5$) the nulling point shifts to about $1.55\Phi_0$ for an inductance ratio $\alpha_J = L_s/L_{J0} \simeq 0.25$ applicable to JM₁.

Similar to the tunable bandwidth measurement of JM₁ shown in Fig. 4 (a) and (b), we plot in Fig. 6 (a) and (b), the reflection amplitudes S_{aa} and S_{bb} versus frequency measured for multiple working points of JM₂. The measured curves are normalized by the pump off data. Samecolor curves in (a) and (b) are taken at the same working point. As seen in the plots both modes exhibit a tunable range of about 600 MHz. In the table beneath panels (a) and (b), we list a bandwidth proxy for each of the working points, which we adopt due to the relatively large ripples in the measured reflection response, which are caused by standing waves forming in the coaxial lines between the circulators and the device (see setup diagram in Fig. 18 and Appendix G for more details). The proxy bandwidth values listed in the table are rounded down to the nearest tens of megahertz and correspond

to the frequency span for which the reflection amplitude curves lie primarily below -10 dB and roughly cover the range in which appreciable frequency conversion is taking place in the JM. In Fig. 6 (c) and (d), we contrast the frequency response of S_{aa} and S_{bb} measured for the same working point (green in (a) and (b)) using two different input powers, i.e., -135 dBm (black) versus -95 dBm (red). As seen in the figure, the two measured frequency responses of the JM exhibit near perfect overlap despite applying a 40 dB higher input power than in the low power case. To further quantify the saturation power of the device at this working point, we exhibit in Fig. 6 (e) and (f) saturation power measurements taken at 7.247 GHz and 10.22 GHz, respectively, which yield maximum input powers of -100 dBm for port a and at least -89dBm for port b.

The considerably higher saturation powers (by 20-40 dB) measured in JM_2 compared to JM_1 can be attributed, to a large extent, to their different mode of operation, frequency conversion without photon gain versus amplification and also to possibly having a much stiffer pump in the conversion case, as their applied pump frequencies are vastly different, i.e., around 3 GHz in conversion versus 17 GHz in amplification.

In Fig. 6 (g) and (h), we plot another working point of JM_2 (drawn in blue in panels (a) and (b)), which yields the largest effective bandwidth of about 670 MHz and 740 MHz, respectively. Using the transfer matrix model of the JM and the device parameters listed in Table II, we calculate the reflection (S_{aa}, S_{bb}) and conversion param-

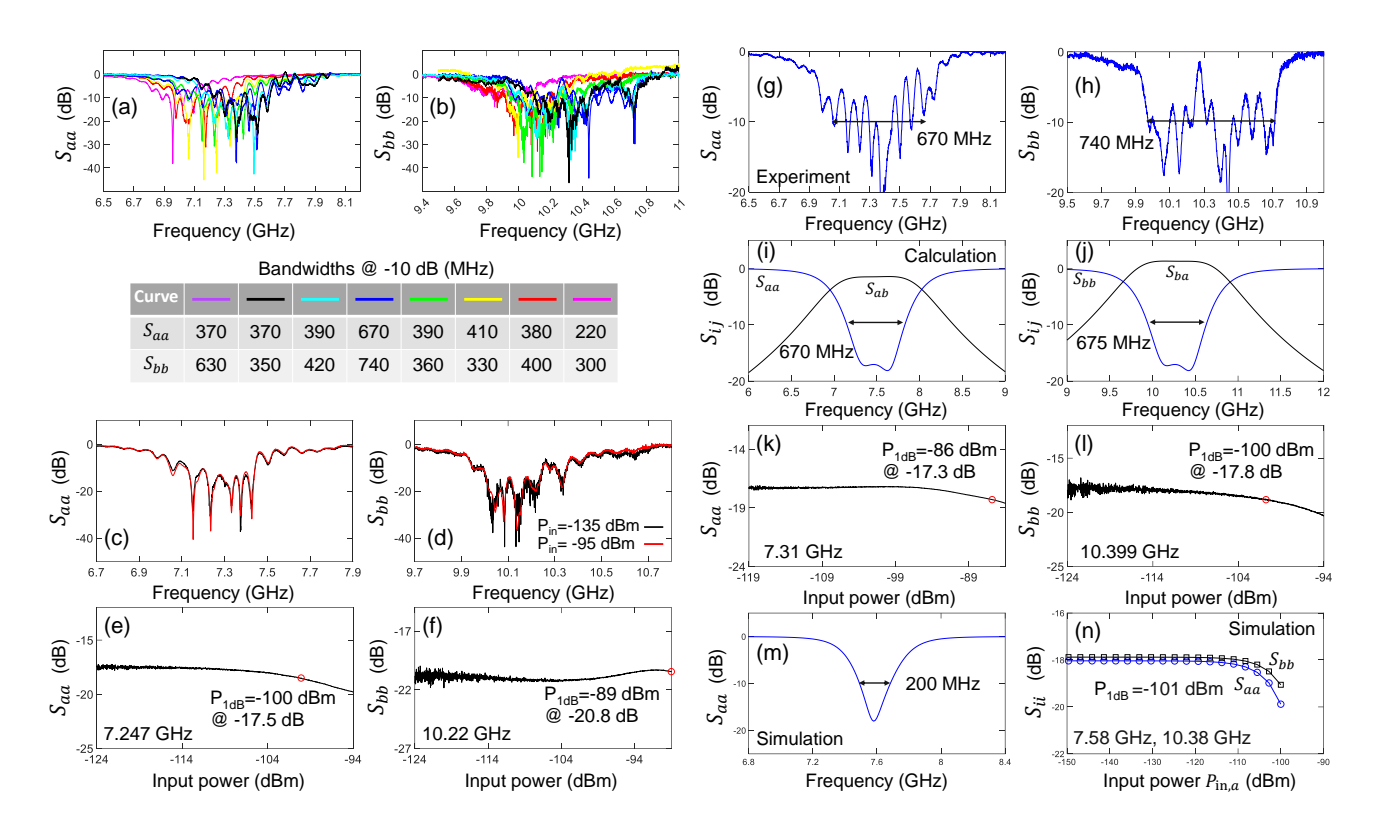


FIG. 6. (a) and (b) reflection magnitude measurement results S_{aa} and S_{bb} of JM₂ taken for different working points set by the applied flux, pump frequency, and power. Curves of the same color in (a) and (b) are taken at the same working point. The table beneath (a) and (b) lists a bandwidth proxy of the various working points for mode a and b taken at -10 dB. The values in the table are rounded down to the nearest tens of Megahertz. (c) and (d) exhibit measured reflection magnitude curves (black) for one of the working points drawn in green in (a) and (b). The red curves which mostly overlap with the black curves correspond to the same working point measured at higher input power, i.e., -95 dBm versus -135 dBm. (e) and (f) saturation power measurements taken at 7.247 GHz (S_{aa}) and 10.22 GHz (S_{bb}) for the working point of (c) and (d). (g) and (h) exhibit measured reflection magnitude curves for one of the working points drawn in blue in (a) and (b) (with the largest bandwidth). The frequency range listed on the plots represent a bandwidth proxy taken at -10 dB. (i) and (j) calculated scattering parameters of the device, S_{aa} and S_{bb} in blue and S_{ab} and S_{ba} in black. The theoretical model used in the calculation employs the extracted parameters listed in Table II. (k) and (l) saturation power measurements taken at 7.31 GHz (S_{aa}) and 10.399 GHz (S_{bb}) for the working point of (g) and (h). (m) Keysight ADS simulation of the reflection magnitude S_{aa} versus frequency. (n) Keysight ADS simulation of S_{aa} (blue circles) at 7.58 GHz and S_{bb} (black squares) at 10.38 GHz versus the signal power applied to port a.

eters versus frequency (S_{ab}, S_{ba}) plotted in Fig. 6 (i) and (j) using blue and black curves, respectively. As seen in the figure, we obtain an effective bandwidth of about 670 MHz, which is similar to the experimental value. Note that the different maximum levels of the calculated transmission parameters between S_{ba} (1.29 dB) and S_{ab} (-1.45 dB) originate from the Manely-Rowe relations [55, 56], requiring power gain (reduction) in upconversion (downconversion) processes that have unity photon gain, which correspond to the ratio of the output to the input frequency $10 \log_{10} (\omega_b/\omega_a) = 1.38 \text{ dB}$ (-1.38 dB).

In Figs. 6 (k) and (l) we exhibit the corresponding saturation power measurements for the working point of (g) and (h), which yield at about -17 dB for mode a and b, -86 dBm and -100 dBm, respectively. The simulated response S_{aa} versus frequency near this working point is

shown in Fig. 6 (m). While the simulation result exhibits a considerably narrower bandwidth than in the experiment, i.e., 200 MHz versus 670 MHz, the simulated saturation power shown in Fig. 6 (n) yields a fair agreement with the experimental value for mode b.

One interesting aspect of the measurement results shown in Figs. 4 and 6, is that despite having the same design, $\rm JM_1$ and $\rm JM_2$ exhibit large disparity in their typical measured bandwidths, i.e., tens versus hundreds of megahertz, which stem from their different mode of operation, i.e., amplification versus conversion. While in amplification, the JM follows the amplitude-gain bandwidth product limit, which results in decreased bandwidth with gain, in conversion it follows a similar limit for only one possible bandwidth metric. To elucidate this key distinction, we plot in Fig. 7(a) a calculated response of an ideal

resonant-mode JM operated in conversion (see Appendix F). The plot exhibits the reflection (red) and frequency-converted transmission (blue) amplitudes versus normalized frequency deviation, where f_0 is the resonance frequency of mode a or b of the JM. As illustrated in the plot, it is possible to define three bandwidth metrics: (1) frequency spacing of the reflection parameter at +3 dB (or any desired +X dB) above the on-resonance minimum, (2) frequency spacing of the reflection parameter at -3 dB (or any desired -X dB) below the off-resonance 0 dB level, and (3) frequency spacing of the transmission parameter at -3 dB (or any desired -X dB) below the on-resonance maximum.

To demonstrate how the shapes of the reflection and transmission curves change with pump power, we plot in Fig. 7(b) the calculated JM response for varying pump amplitudes. As seen in the plot, the transmission and reflection curves calculated using Eq. (F2) and Eq. (F4), become wider with the increased pump, while the reflection minimum becomes smaller and narrower. To quantify this effect, we plot in Fig. 7(c), the three extracted bandwidths based on the three metrics outlined above as a function of the normalized pump power ρ^2 . As expected, the red curve associated with the reflection minimum decreases with the pump, while the black and blue curves associated with reflection and transmission maxima increase with pump and converge at a value that is close to the larger linear bandwidth of modes a and b. We also plot for reference in Fig. 7(d), the corresponding maximum transmission (blue) and minimum reflection (red) parameters.

V. COUPLED-MODE JOSEPHSON MIXERS

In this section, we present measurement results taken for the coupled-mode JM design, i.e., JM₃ and JM₄, which are operated in amplification and frequency-conversion, respectively.

To enhance the bandwidths of JM devices, especially of parametric amplifiers which are inherently limited by the amplitude-gain bandwidth product, we apply the versatile and quite effective technique for shaping the frequency response of microwave devices known as impedance matching, which can be realized by incorporating coupled-mode networks between the parametric nonlinear element and the external feedlines.

While there is a large number of useful references that apply impedance matching methods in a wide variety of microwave applications [56–60], here we apply the design technique of coupled-mode networks outlined and distilled in Ref. [41] for Josephson junction-based parametric devices. However, since the emphasis in that reference is on grounded SQUID-based parametric devices, we extend the prescribed engineering procedure for multinode Josephson element such as the JRM, which cannot be grounded without sacrificing its critical ability to support nondegenerate modes.

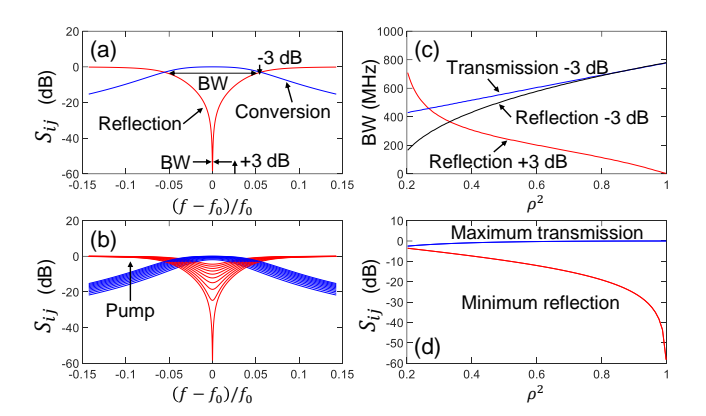


FIG. 7. (a) Amplitudes of reflection (red) and transmission with frequency conversion (blue) of an ideal resonant-mode JM plotted versus normalized frequency. The two curves are calculated using Eq. (F4) and Eq. (F1). The plot serves to illustrate three possible bandwidth figures: (1) frequency difference between the -3 dB points of the reflection curve relative to the 0 dB off-resonance level, (2) frequency difference between the -3 dB points of the conversion curve relative to the maximum transmission on resonance, and (3) frequency difference between the +3 dB points relative to the minimum reflection on resonance. (b) same as (a) calculated for an ascending normalized pump power. (c) displays the dependence of the three possible bandwidth figures illustrated in (a) as a function of normalized pump power ρ^2 . (d) plots the corresponding maximum transmission with frequency conversion (blue) and minimum reflection (red) as a function of normalized pump power ρ^2 . In the calculation, we employ $f_a = 7$ GHz, $f_b = 10$ GHz, $\gamma_a/2\pi = 400$ MHz, $\gamma_b/2\pi = 900$ MHz.

In Fig. 8 we outline the design scheme that we apply to the JRM case. To better explain the design process, we start from the final coupled-mode circuit design depicted in Fig. 8 (a). In addition to the fundamental modes of the device formed by shunting the JRM and the series outer inductors by lumped-element capacitors, each pair of differential ports a and b incorporates three capacitively-coupled parallel lumped-element LCresonators. This circuit diagram represents an idealized version of JM₃ and JM₄ layout shown in Fig. 2 (b) and (d) with two main differences that are introduced for pedagogical purposes. First, we substitute the single shunt capacitor on each side of the JRM with two capacitors in series with double the capacitance. Second, we join the respective grounded LC resonators on each arm of port a and b via their common ground connection. Such changes highlight the structural symmetry that exists in the device including the JRM with respect to the virtual ground that passes through the middle of each pair of differential ports as indicated by the dashed blue and green lines. By taking half of the circuit extending along the virtual ground of both modes shown in Fig. 8 (b), we can cast the coupled-mode network of the JM in the standard grounded form used in Ref. [41], which incorporates admittance inverters $J_{ij,k}$ between resonators i

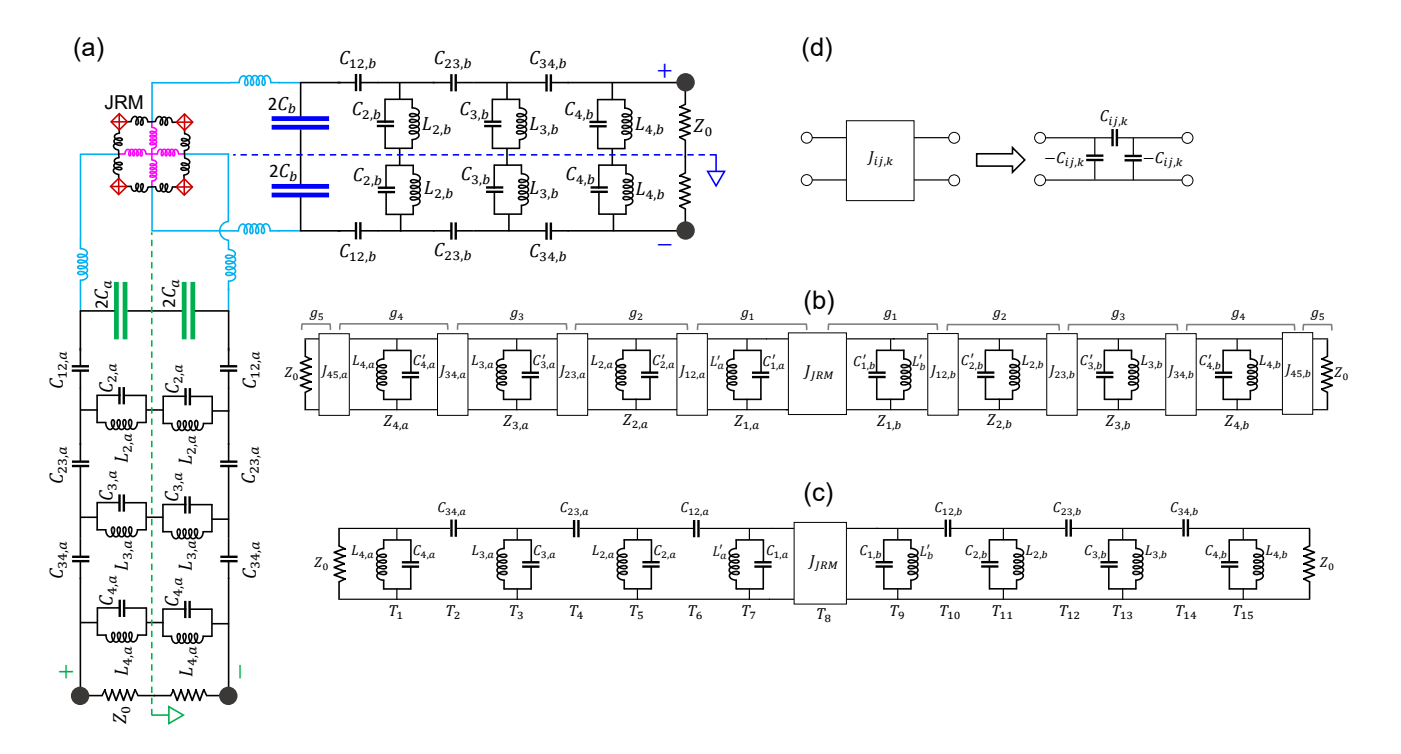


FIG. 8. (a) Circuit model of the Josephson mixers with lumped-element, impedance matching networks, i.e., JM_3 and JM_4 . In this model, we replaced the single capacitor shunting opposite nodes of the JRM (shown in Fig. 2 (b) and (d)) with an equivalent fictitious two capacitors in series with double the capacitance, and joined the respective LC resonators shorted to ground between ports A_1 and A_2 and B_1 and B_2 via a common virtual ground that passes through the symmetry axes of the differential modes of the JRM (indicated by dashed green and blue lines). (b) exhibits a circuit model in which half of the JRM represented as an admittiance inverter J_{JRM} is matched to the external feedlines via a series of parallel LC resonators and admittance inverters $J_{ij,k}$. (c) forms the basis for (a) and it is derived from (b) after substituting the generic admittance inverters $J_{ij,k}$ with their corresponding lumped-element capacitive π sections illustrated in (d) and absorbing any negative capacitance associated with these sections into the shunt capacitors of the LC resonators.

and j belonging to mode k. Each resonator i of mode k is characterized by an impedance $Z_{i,k}$. The values of $J_{ij,k}$ are determined by the prototype coefficients of the filter design g_i and g_j and the impedances of the adjacent resonators (see Appendix C.1). After replacing the generic admittance inverters in Fig. 8 (b) with a circuit realization in the form of lumped-element capacitive π sections illustrated in Fig. 8 (d), we obtain the desired circuit design parameters outlined in (c) (which form the basis of the final design presented in (a)).

To calculate the JM response, we multiply the ABCD matrices of the various elements of the circuit represented by T_i . The ABCD matrices of the coupling capacitor and parallel LC resonators are shown in Fig. 9, whereas that of the JRM, which depends on the JM mode of operation, is shown in Fig. 3.

In Fig. 10 (a) and (b), we exhibit S_{aa} and S_{bb} of JM₃ measured versus frequency for pump on (blue) and off (black). Both measurement results are normalized relative to the calibrated reflection data measured in-situ for a short termination (red). As seen in the figure, the amplification gain measured on ports a and b exceed 10 dB within a bandwidth of 410 MHz and 390 MHz, respec-

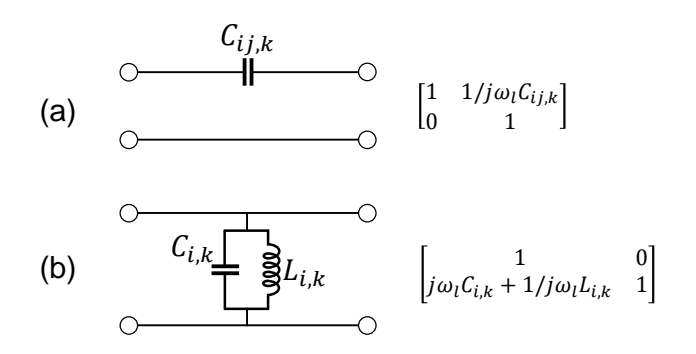


FIG. 9. The corresponding ABCD (T) matrices for a series capacitor $C_{ij,k}$ coupling stages i and j of mode k (a) and LC resonator i of mode k (b).

tively. Amplitude dips observed in the device response outside the device bandwidth could originate from unmatched fabricated values of one or two LC resonators along the symmetry lines of the device (shown in Fig. 8 (a)), causing some of the energy of the excited differential

mode at the dip frequencies to leak into a common mode, which gets absorbed by the cold 50 Ohm termination attached to the Σ port of the hybrid employed in the experimental setup (Fig. 18). Using the device parameters listed in Table IV and the transmission matrix model of the device, we plot in Fig. 10 (c) and (d), the calculated amplification curves for the ideal lossless device, which yield a qualitative agreement with the measurement and a bandwidth of 450 MHz at 10 dB.

Saturation power measurements taken in band at the same working point are shown in Fig. 10 (e) and (f) for port a and b, respectively. The gain curves plotted versus input power are normalized relative to the pump-off data. As seen in the plots, the coupled-mode JM achieves saturation powers of -110 dBm at 7.675 GHz and -106dBm at 10.745 GHz, which are comparable to saturation powers attained by some TWPAs [30, 31] and are at least 23 dB higher than typical values measured for JM₁ (shown in Fig. 4) and resonant-mode JMs implemented using transmission-line resonators [49]. In Figs. 10 (g) and (h), we plot simulation results for the JM device obtained using harmonic-balance in Keysight ADS. In subplot (g), we depict the amplification response of the JM versus frequency obtained on port a, which, similar to the calculated response, yields a qualitative agreement with the measurement, however with a lower bandwidth of 350 MHz at 10 dB. Likewise, the simulated gain versus input power shown in Fig. 10 (h) yields a saturation power of -116 dBm, which is 6 dB lower than the measured value. It also features a "shark-fin" behavior which is absent in the data.

To further demonstrate that JM₃ operates near the quantum noise limit, we measure the noise rise G_N of the output chain for port a and b as a function of the device gain G. Selected amplification curves measured for different pump powers are shown in Figs. 11 (a) and (e), which correspond to ports a and b, respectively. An example of G_N versus frequency measured for one of the working points in (a) and (e) is drawn in panels (b) and (f). By plotting the SNR improvement G/G_N , versus gain (blue dots) measured at 7.818 GHz and 10.655 GHz (shown in panels (c) and (g)), and fitting the data using Eq. (H2) (black), we obtain estimates for the effective noise temperature of the output lines T_N (which are consistent with the expected values for the setup) and the added noise by the JM (referred back to the input), i.e., $n_{\rm add}$ in the range 0.5 – 0.6. Finally, we show in (d) and (h), the SNR improvement versus frequency (blue) plotted for the same working point (pump power) as (b) and (f). The black curves are theory fits, which employ the same extracted parameters displayed in (c) and (g).

Key measurement results obtained using JM_4 are shown in Figs. 12 and Figs. 13. In Fig. 12 (a) and (b) we exhibit the amplitude response of S_{aa} and S_{bb} versus frequency measured with pump on (blue) and off (black). Both measurements are normalized relative to the calibrated reflection data measured in-situ for a short termination (red). Relatively wide bandwidth of about 700

MHz and 860 MHz is observed at -10 dB for the pump on measurement in panels (a) and (b), respectively. A comparable wide bandwidth of about 765 GHz at -10 dB is seen in the calculated response of the device (blue) displayed in Fig. 12 (c) and (d). Similar to the calculated response of JM₂ shown in Fig. 6 (i) and (j), we calculate the scattering parameters S_{ij} of JM₄ using the transmission matrix model outlined in Figs. 3 and 8, and the device parameters listed in Table V. Saturation power measurements corresponding to the working point of (a) and (b) are depicted in Fig. 12 (e) and (f), respectively. Relatively high saturation powers of -91 dBm and -110 dBm are measured for reflection parameters $S_{aa} = -26$ dB and $S_{bb} = -28$ dB, respectively.

In Figs. 12 (g) and (h), we exhibit, for comparison, Keysight ADS simulation results obtained for the circuit model of JM₄. Similar to the calculated S_{aa} amplitude versus frequency shown in (c), the simulation result in (g) exhibits a qualitative agreement with the experimental data shown in (a) and yields a bandwidth of about 620 MHz at -10 dB, which is comparable to the measured value 700 MHz. Panel (h) exhibits a simulation result of the saturation power at 7.66 GHz (blue circles) and 10.67 GHz (black squares) for the same working point and device parameters shown in (g). While the simulated response does not capture the rise of S_{aa} and S_{bb} with input power seen in panels (e) and (f), it yields a saturation power of -97 dBm, which lies close to the typical range of -95 dBm to -90 dBm measured for the device (as seen in Fig. 12 (e), and also in Fig. 13(c), (d)).

Similarly, in Fig. 13 we show measurement results of another working point of JM₄ taken at a slightly different flux and pump frequency than Fig. 12 (see Table VII). While the normalized pump-on reflection parameters S_{aa} (a) and S_{bb} (b) exhibit narrower bandwidths, i.e., 320 MHz and 360 MHz, the measured saturation powers -93 dBm and -95 dBm displayed in (c) and (d) are quite similar to the measured value in Fig. 12 (e).

VI. DISCUSSION

The results outlined above show that nondegenerate JM devices operating near the quantum limit can achieve large bandwidth and high saturation power, both in amplification and transduction.

In particular, we obtain bandwidth enhancement in conversion using two design schemes: (1) realizing low external quality-factor, lumped-element, resonant-mode JM devices that are strongly coupled to the external feedlines of modes a and b, and (2) applying impedance matching between the JRM and the external feedlines, by incorporating lumped-element coupled-mode networks. Using the first method, we demonstrate tunable bandwidth of about 600 MHz for both modes and dynamical bandwidths in the range 220 – 740 MHz with calibrated reflection parameters below –10 dB. Using the latter scheme, we achieve at the optimal point, dynami-

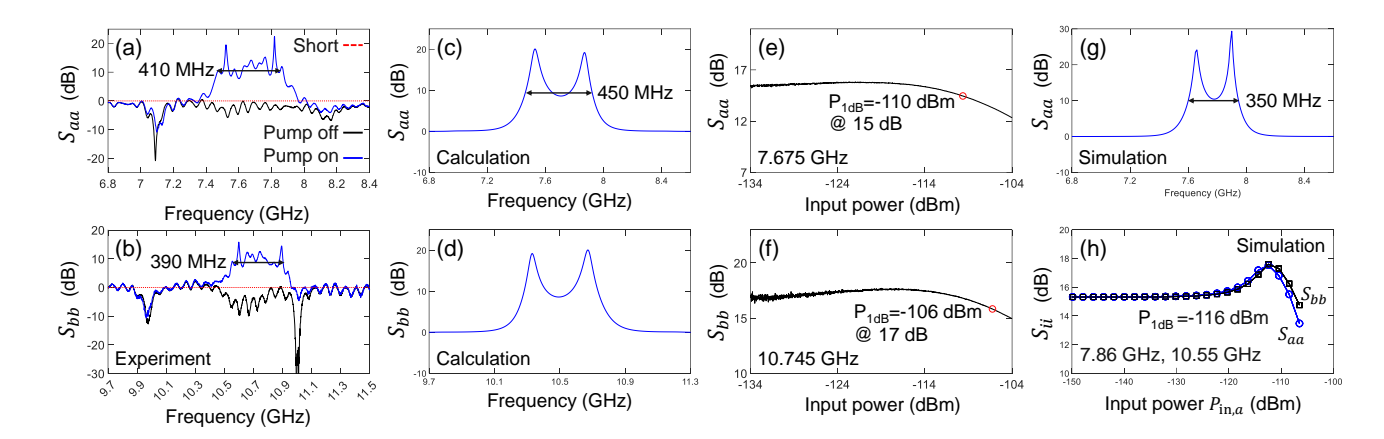


FIG. 10. (a) and (b) reflection gain curves S_{aa} and S_{bb} (blue) of JM₃ measured versus frequency (pump on). The black curves are reflection magnitude for mode a and b measured versus frequency with pump off. Both results are calibrated relative to the reflection magnitude measured for a short ended setup plotted as a 0 dB guide-to-the-eye dashed red line. The frequency range listed on the plots represent a bandwidth proxy taken at 10 dB. (c) and (d) calculated gain versus frequency for mode a and b. The theoretical model employs the extracted parameters of the device listed in Table IV. (e) and (f) saturation power measurements taken at 7.675 GHz and 10.745 GHz for the working point of (a) and (b). (g) Keysight ADS simulation of the reflection gain S_{aa} versus frequency. (h) Keysight ADS simulation of S_{aa} (blue circles) at 7.86 GHz and S_{bb} (black squares) at 10.55 GHz versus the signal power applied to port a.

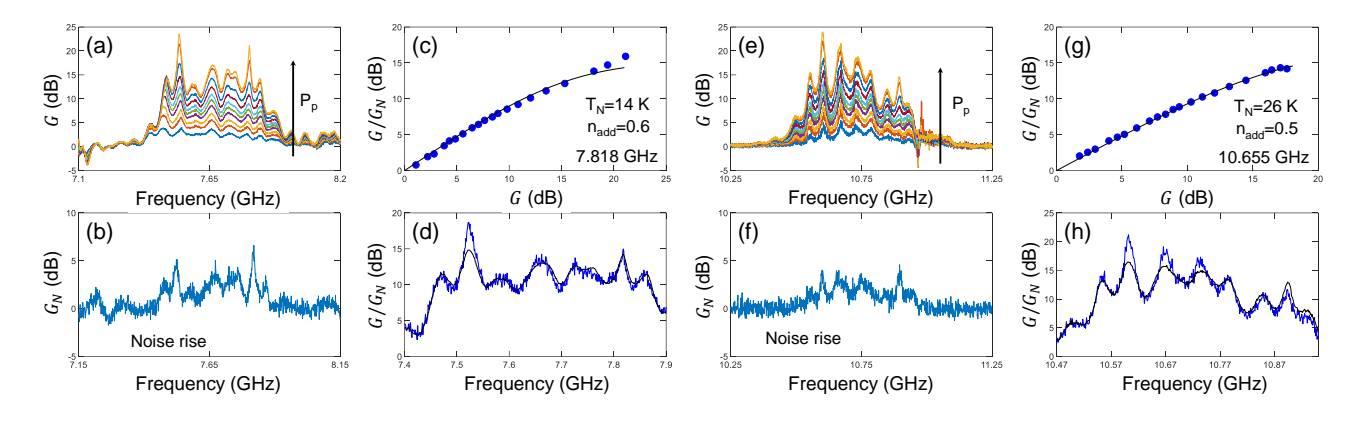


FIG. 11. (a) Gain curves measured for mode a of JM₃ versus frequency for ascending pump power, normalized by the pump off data. (b) Noise rise versus frequency measured for one of the working points shown in (a). (c) SNR improvement versus gain (filled blue circles) measured at 7.818 GHz. The black curve is a theory fit that employs $T_{\rm N}$ and $n_{\rm add}$ listed in the plot. (d) SNR improvement for a fixed gain plotted versus frequency (blue). The black curve is a theory fit that uses the same $T_{\rm N}$ and $n_{\rm add}$ listed in (c). (e)-(h) same as (a)-(d) obtained for mode b of JM₃

cal bandwidths of about 700 MHz and 860 MHz on ports a and b corresponding to calibrated reflection parameters below -10 dB. Similarly, we achieve bandwidth enhancement in amplification using the coupled-mode method, which yields at the optimal point, dynamical bandwidths of about 410 MHz and 390 MHz for mode a and b with calibrated reflection gains above 10 dB.

For comparison, state-of-the-art resonant-mode JM devices that employ microstrip resonators achieve dynamical bandwidths of about 3-10 MHz at 20 dB of gain in amplification [26, 51], and about 10-20 MHz at -20 dB of reflection in conversion [22]. Thus, the band-

width obtained using the couple-mode method amounts to an enhancement by approximately a factor of 40 in amplification and 30 in conversion.

Likewise, we achieve concurrent enhancements in the saturation power using several methods. In the case of the resonant-mode JM design, we (1) flux bias the JRM near the Kerr-nulling working point, and (2) dilute the nonlinearity of JRMs by incorporating outer inductors in series with the JRM, thus reducing the participation ratios, and by shunting the JJs of the JRM with relatively small linear inductors (L_{in}) , which yield $\beta \cong 3.6$. Similarly, in the case of the coupled-mode JM design, we

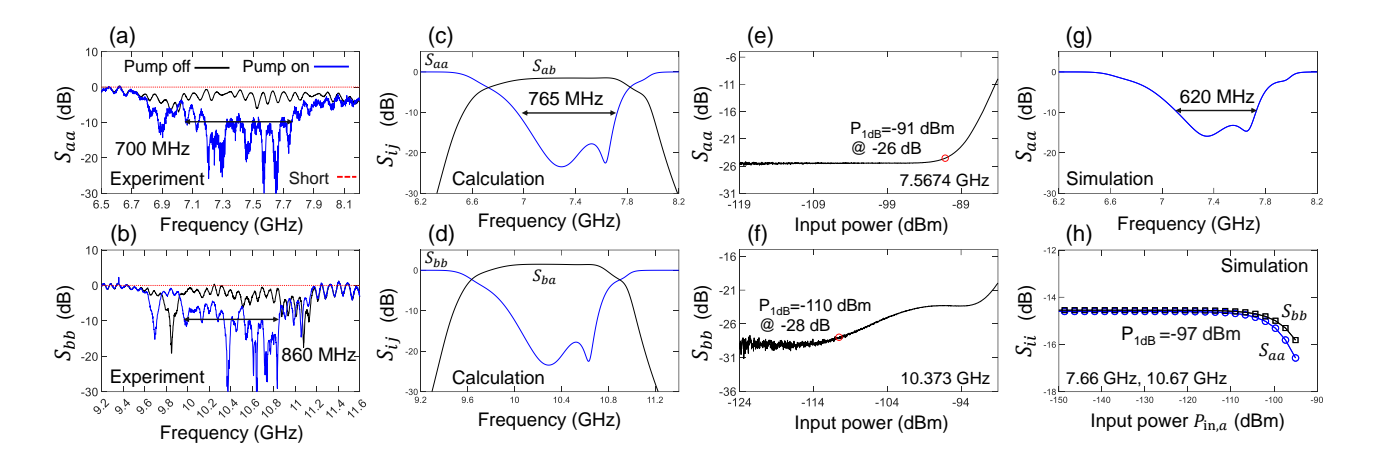


FIG. 12. (a) and (b) reflection magnitude S_{aa} and S_{bb} measured versus frequency for JM₄ with pump on (blue) and pump of (black). Both measured curves are calibrated relative to the reflection magnitude measured for a short ended setup plotted as a 0 dB guide-to-the-eye dashed red line. The frequency range listed on the plots represent a bandwidth proxy taken at -10 dB. (c) and (d) calculated scattering parameters of the device, S_{aa} and S_{bb} in blue and S_{ab} and S_{ba} in black. The different maximum levels of S_{ba} (1.47 dB) and S_{ab} (-1.51 dB) stem from the frequency conversion process taking place without photon gain. They are also in line with the predictions of the Manely-Rowe relations [55], i.e., $10 \log_{10} (\omega_b/\omega_a) = 1.48$ dB and $10 \log_{10} (\omega_a/\omega_b) = -1.5$ dB, respectively. The theoretical model used in the calculation employs the extracted parameters listed in Table V. (e) and (f) saturation power measurements taken at 7.5674 GHz (S_{aa}) and 10.373 GHz (S_{bb}) for the working point of (a) and (b). (g) Keysight ADS simulation of the reflection magnitude S_{aa} versus frequency. (h) Keysight ADS simulation of S_{aa} (blue circles) at 7.66 GHz and S_{bb} (black squares) at 10.67 GHz versus the signal power applied to port a.

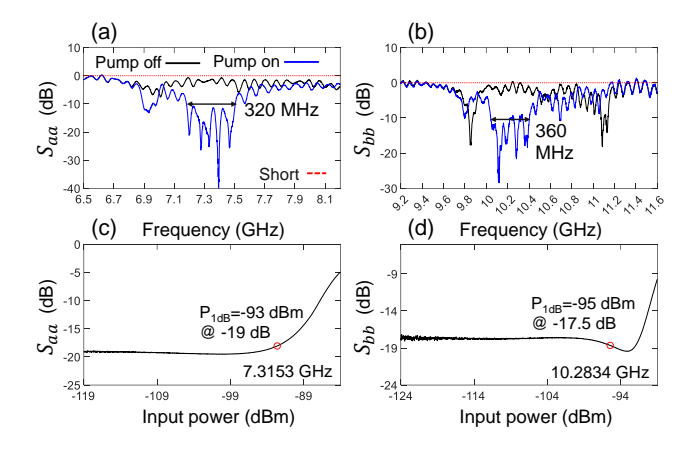


FIG. 13. Another measured working point of JM₄. (a) and (b) show the reflection magnitude S_{aa} and S_{bb} measured versus frequency for JM₄ with pump on (blue) and pump off (black). Both measured curves are calibrated relative to the reflection magnitude measured for a short ended setup plotted as a 0 dB guide-to-the-eye dashed red line. The frequency range listed on the plots represent a bandwidth proxy taken at -10 dB. (c) and (d) saturation power measurements taken at 7.3153 GHz (S_{aa}) and 10.2834 GHz (S_{bb}) for the working point of (a) and (b).

(1) set the parameters of the LC resonators to match a capacitively-shunted JRM operated near the Kerr-nulling working point, (2) dilute the nonlinearity of the JRM by employing $\beta \cong 4.4$, and (3) reduce the pump power

needed to attain a desired magnitude of reflection parameters. The latter is a direct result of adding linear LC resonators to the device (i.e., by increasing the order of the "filter" employed in the implementation) [41].

By utilizing these techniques, we measure in the amplification case of the resonant-mode JM, maximum saturation powers of about -118 dBm at 20 dB of gain. While in the conversion case, we measure as expected, higher saturation powers in the range of -100 dBm to -86 dBm at a reflection of about -17 dB.

Further enhancement in the saturation power in amplification, by about 10 dB, is obtained in the coupled-mode JM design, which achieves about -110 dBm and -106 dBm for port a and b at gains of about 15 dB and 17 dB, respectively. When compared to typical saturation powers in the range -135 dBm to -125 dBm achieved in microstrip-based JM devices [26, 49], the results of the coupled-mode JM amounts to about 15-29 dB enhancement. Also, notably the achieved saturation power in the coupled-mode design of about -106 dBm is on par with saturation powers measured in typical TWPAs in the range -110 dBm to -100 dBm [30, 31], while using only 4 JJs with modest critical currents 2.5 $\mu \rm A$, as opposed to, for example, a chain of about 2000 JJs with 4.6 $\mu \rm A$ each [30].

Similarly, in conversion, we achieve using the coupled-mode JM design high saturation powers in the range -95 dBm to -91 dBm, measured at a reflection of about -18 dB to -26 dB.

With such enhancements in the bandwidths and saturation powers, it is interesting to estimate the number of

readout signals that can be multiplexed in amplification and conversion using the coupled-mode JMs. Assuming an average frequency spacing between the readout signals of about 70 MHz, set to ensure an acceptable level of crosstalk in the quantum chip, we obtain in the amplification (conversion) case about 6 (11) signals. Whereas, if we only consider the attainable saturation power while ignoring the bandwidth limitation, and assuming low-power readout, the number of signals which the JMs can potentially process is considerably higher, on the order of tens in amplification and hundreds in conversion.

Among the disadvantages of lumped-element coupledmode JMs are: (1) they have numerous design parameters that need to be accurately set within a few percent to obtain a near ideal response. For example, in the JM₃ and JM₄ designs, there are about 22 capacitance and inductance parameters. This makes the response of these devices sensitive to systematic errors in the design (such as underestimating or overestimating the values of the lumped-inductances and capacitances), and sensitive to random fabrication variations of these parameters, especially the capacitances. Moreover, these parameters are not independent, therefore a variation in one can have an unexpected effect on the rest of the circuit. (2) Their response get degraded compared to the ideal lumpedelement circuit design due to unintentional parasitic inductances and capacitances forming inside or between sections due to layout limitations. (3) Any mismatch in their lumped-element capacitors and inducators realized along the two arms of M_k , i.e., J_1 - K_1 and J_2 - K_2 (see Fig. 1 (c)), breaks the device symmetry and negatively impacts the differential excitation applied to port k.

It is feasible, however, to overcome and minimize the effect of the first two disadvantages by applying multiple iterations of design, fabrication, and measurement, and by further tightening the variability of the fabrication process. Similarly, it is possible to significantly mitigate the third drawback by combining the respective pairs of capacitive and inductive elements along the two arms of the impedance-matching units M_k , and differentially excite these units using on-chip 180 degree hybrids.

Moreover, since the insertion loss in our devices varying in the range $0-5~\mathrm{dB}$ is dominated by dielectric loss, this figure can be improved by reducing the dielectric loss of the insulating layers employed in the plate capacitors or replacing them with higher Q materials.

Finally, it is worth noting that the dynamical bandwidth of JM_2 can be easily enhanced further by reducing the imbalance in the linear bandwidths of mode a and b, i.e., 347 MHz, and 912 MHz, respectively, which stems from the difference between C_a and C_b . One straightforward method to achieve that is by reducing the impedance of the external feedlines of port a by half (and therefore reducing the external quality factor of mode a by the same amount), which can be implemented for example by incorporating a quarter-wavelength transformer of impedance 35 Ohm along the arms of the impedance-matching unit connected to port a (Fig. 1(b)).

VII. CONCLUSION AND OUTLOOK

We introduced a blueprint for building large bandwidth and high saturation power lumped-element nondegenerate JMs capable of processing microwave signals near the quantum limit. We implemented the new JM designs using a fabrication process that is based on trilayer Nb junctions and plate capacitors, and introduced a novel transmission line design for pumping the device through a separate port. In particular, we fabricated and measured two JM devices operated in amplification and another two operated in frequency conversion. We achieved significant bandwidth enhancement in the amplification and conversion mode of operation in two JM devices by incorporating impedance-matching networks between the capacitively shunted JRMs and the external feedlines. We realized these impedance-matching networks using coupled-mode networks made of capacitively-coupled LC resonators. We also demonstrated bandwidth enhancement in conversion by realizing a low external quality factor lumped-element, resonant-mode JM device.

Furthermore, we enhanced the saturation power of the JM devices, by diluting the JRM nonlinearity and designing the coupled-mode networks of the JM devices to have multiple modes per port and operate as close as possible to the Kerr-nulling working point of the JRM.

Such impedance-matched nondegenerate JM devices, which have enhanced bandwidths of hundreds of megahertz and saturation powers in excess of -100 dBm could be useful in a wide range of quantum applications, such as (1) performing fast, frequency-multiplexed, high-fidelity qubit readout in large quantum processors [5, 39, 61], (2) serving as wideband and bright sources of continuous-variable entanglement in modular quantum computing architectures and quantum networks [62–65], (3) enabling quantum illumination in the microwave domain [66, 67], (4) converting quantum signals from one microwave frequency band to another, and (5) forming nonreciprocal low-loss on-chip Josephson devices that are essential for scaling up quantum systems [21, 22].

ACKNOWLEDGMENTS

We are grateful to John Walter, Jake Fonseca, Khanh Dang, and J. R. Rozen for technical support, Michael Beckley, Charles Rettner, Teddie Magbitang, and Bryan Trimm for preliminary device fabrication, and David Lokken-Toyli, Matthew Beck, and Gerald Gibson for helpful discussions.

B.A. designed and simulated the devices, performed the measurements, and analyzed the data. D.S. designed the layout, S.C. fabricated the devices, J.N. bump bonded the devices, O.J. contributed to the experimental setup, S.S. and T.M. designed and simulated layout components, V.A. designed the printed circuit boards, C.M. simulated earlier designs and supervised the project. B.A. wrote the paper with input from the

other authors.

The authors declare no competing interests.

Appendix A: Mutual inductance of the JRM

For the JM, the mutual inductance between modes a and b is primarily parametric with no passive component, $M_0 = 0$. Thus, it can be written as

$$M(t) = \delta M \cos(\omega_p t)$$

$$= \frac{\delta M e^{j\omega_p t} + \delta M^* e^{-j\omega_p t}}{2}, \quad (A1)$$

where ω_p is the angular frequency of the pump drive and δM is the mutual inductance modulation amplitude, which we infer from the inductive energy of the JRM given by [28]

$$E_{\rm JRM} = \frac{1}{2} L_J \left(I_1^2 + I_2^2 + \frac{1}{4} I_p^2 \right) - \frac{1}{4} \frac{L_J I_\phi}{I_0^2} I_1 I_2 I_p, \ \ ({\rm A2})$$

where I_1 and I_2 are the rf currents of mode a and b respectively, I_p is the rf current of the pump drive, and I_0 is the critical current of the JJs.

By casting Eq. (A2) in the equivalent form

$$E_{\text{JRM}} = \frac{1}{2} L_J \left(I_1^2 + I_2^2 + \frac{1}{4} I_p^2 \right) - \frac{1}{2} M(t) I_1 I_2, \quad (A3)$$

we obtain

$$\delta M = \frac{1}{2} \frac{L_J I_\phi}{I_0^2} \left| I_p \right|, \tag{A4}$$

where

$$I_{\phi} = I_0 \sin\left(\varphi_J\right),\tag{A5}$$

is the circulating current in the outer loop of the JRM, $L_J = L_{J0}/\cos{(\varphi_J)}$ is the inductance of the JJs, $L_{J0} = \varphi_0/I_0$ is the JJ inductance at zero external flux, $\varphi_0 = \Phi_0/2\pi$ is the reduced flux quantum, and φ_J is the superconducting phase difference across the JJs which can be approximated as [51]

$$\varphi_J = \frac{\varphi_e}{4} - \alpha_J \sin\left(\frac{\varphi_e}{4}\right) + \frac{1}{2}\alpha_J^2 \sin\left(\frac{\varphi_e}{2}\right), \quad (A6)$$

where $\varphi_e = \Phi_e/\varphi_0$, Φ_e is the external flux threading the JRM loop, and $\alpha_J = L_s/L_{J0}$.

Based on the extracted parameters of the different designs listed in Tables II, IV, and V, we estimate $\alpha_J \simeq 0.25$ in the case of JM₁ and JM₂, and $\alpha_J \simeq 0.08$ in the case JM₃ and JM₄.

In general, choices for L_{J0} , L_{in} , L_{out} are made based on design considerations such as optimizing the saturation power of the device or its frequency tunability range. Other factors which play a role in setting their values are layout constraints such as physical spacings between components. These constraints also inevitably set the parasitic inductances L_s in the JRM loop.

Appendix B: Resonant-mode JM design

1. Flux tunability

Based on Fig. 1(a), the inductance of the JRM reads [51]

$$L_{\text{JRM}} = (L_J + L_s) || (2L_{in})$$

$$= \frac{2L_{in} (L_J + L_s)}{L_J + L_s + 2L_{in}}.$$
(B1)

The total inductance of the resonant-mode JM is given by $L_a = L_b = 2L_{out} + L_{JRM}$, where L_{out} is the series inductance connecting the JRM to the shunt capacitors. L_{out} is usually designed to yield a certain participation ratio for the JM given by [52]

$$p = \frac{L_{\text{JRM}}}{L_{\text{JRM}} + 2L_{out}},\tag{B2}$$

or set by the geometric inductance of the leads connecting the JRM to the shunt capacitors as realized in the layout.

For the unpumped resonant-mode JM, the angular resonance frequency of mode k, $\omega_k = 2\pi f_k$, varies with the external applied flux according to

$$\omega_k \left(\varphi_e \right) = \frac{1}{\sqrt{L_k \left(\varphi_e \right) C_k}}.$$
 (B3)

2. Device parameters

To extract the lumped-element circuit parameters of JM_1 and JM_2 devices (introduced in Fig. 1 (a), (b)), we measure the phase response of mode a and b as a function of applied flux Φ_e as shown in Fig. 14, and apply theory fits to the data based on Eq. (B3), which are plotted on top of the data using dashed black curves. The circuit parameters used in the fits are listed in Table II.

To obtain estimates for the internal loss and linear bandwidths of JM_2 , we measure the amplitude and phase of modes a and b shown in Fig. 15, which are taken at the maximum resonance frequency working point. In plot (a) and (c), we exhibit the amplitude of S_{aa} and S_{bb} versus frequency obtained with pump off (blue) and reference curves (green) taken for the same setup and

Parameter	JM_1	$ m JM_2$
I_0 (μ A)	8.1	8.1
L_{J0} (pH)	40.6	40.6
L_s (pH)	10	10
L_{in} (pH)	11.3	11.3
L_{out} (pH)	27	27
C_a (pF)	6.1	5.85
C_b (pF)	3.13	3.13

TABLE II. Circuit parameters of JM₁ and JM₂ devices obtained from the theory fits of the measured frequency response versus applied flux (Fig. 14). The variation in C_a between JM₁ and JM₂ falls within the fabrication variability range.

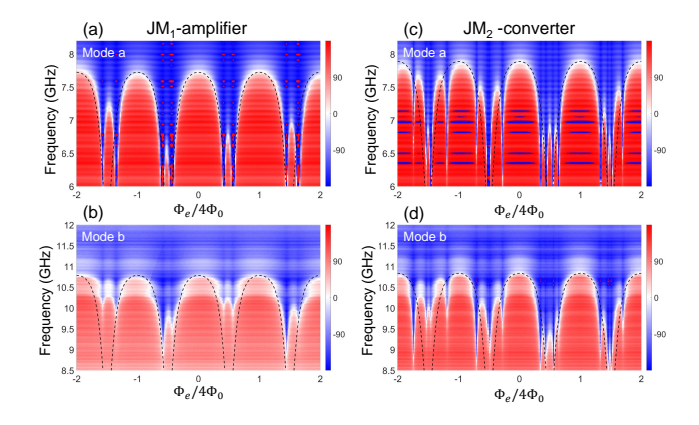


FIG. 14. The measured phase of the reflected signals off ports a and b of JM_1 , shown in (a) and (b) as a function of the normalized external flux. (c) and (d) exhibit similar measurements taken for JM_2 . The resonance frequency of modes a and b follow the zero phase contours. The dashed black curves are theoretical fits to the data obtained using Eq. (B3).

conditions but with open-end terminations (see experimental setup depicted in Fig. 18). As seen in the plots, the off-resonance data (pump off) mostly overlaps with the reference level, however, a deviation of 1 to 4 dB between the curves, likely due to insertion loss in the device, can be observed on resonance. Likewise, in plot (b) and (d) we exhibit the phase of S_{aa} and S_{bb} versus frequency obtained with pump off (blue). By applying a Lorentzian fit (black) to the phase data, we obtain estimates for the linear bandwidths of mode a and b of about 347 MHz and 912 MHz, respectively.

Similar linear bandwidths of about 400 MHz and 1 GHz are measured for mode a and b of JM₁ (as it shares the same design as JM_2).

JM model

To obtain the scattering parameters of resonant-mode JM devices such as, $JM_{1,2}$, we calculate first their transmission (ABCD) matrix, which can be expressed as

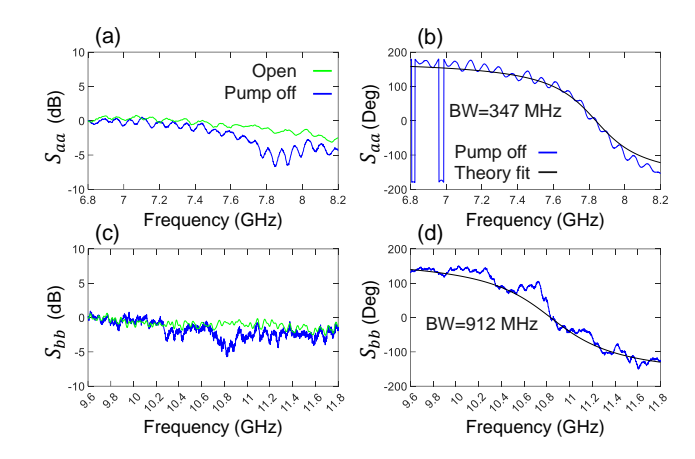


FIG. 15. Amplitude (a) and phase (b) of S_{aa} (blue) measured at the maximum resonance frequency of JM_2 . (c) and (d) same as (a) and (b) for S_{bb} . The green curves in (a) and (c) are reference levels measured for open ends at nominally identical locations as the mounted device. The black curves in (b) and (d) are theoretical fits based on Eq. (F4) and Eq. (F5), which yield linear bandwidths of about 347 MHz and 912 MHz for modes a and b, respectively.

 $T_{\rm total} = T_{\rm a}T_{\rm JRM}T_{\rm b}.$ $T_{\rm JRM}$ is the transmission matrix of the JRM given in Fig. 3(b) for the amplification and conversion modes of operation, whereas T_a and T_b are the transmission matrices of the parallel LC resonators of mode a (i.e., L'_a and C_a) and b (i.e., L'_b and C_b), where $L'_a = L_a (1 - \alpha)$, $L'_b = L_b (1 - \alpha)$, and $\alpha \equiv |\delta M|^2 / 4L_a L_b$.

Both T_a and T_b can be calculated using the transmission matrix of parallel LC circuits listed in Fig. 9(b).

As shown in Fig. 3(b) the transmission matrix of the JRM in the J shunt representation is set by the parameters

$$J_i' = \frac{1}{\omega_i \sqrt{L_a'} L_h'} \sqrt{\alpha} e^{j\phi_p}, \tag{B4}$$

where ϕ_p is the pump phase and i = 1, 2. It is worth noting that when the pump is off $(\alpha = 0)$ $L'_k = L_k$.

After calculating T_{total} for given pump parameters, applied flux, and signal frequency, we obtain the scattering parameters of the JM by substituting the ABCD elements of $\mathbf{T}_{\text{total}}$ into the following known relations [56]

$$S_{aa} = \frac{A + B/Z_0 - CZ_0 - D}{A + B/Z_0 + CZ_0 + D},$$
 (B5)

$$S_{ab} = \frac{2(AD - BC)}{A + B/Z_0 + CZ_0 + D},$$

$$S_{ba} = \frac{2}{A + B/Z_0 + CZ_0 + D},$$
(B6)

$$S_{ba} = \frac{2}{A + B/Z_0 + CZ_0 + D},$$
 (B7)

$$S_{bb} = \frac{-A + B/Z_0 - CZ_0 + D}{A + B/Z_0 + CZ_0 + D}.$$
 (B8)

Appendix C: Coupled-mode JM design

1. JM model

Extending the instantaneous (dynamical) bandwidth of Josephson-based amplifiers beyond the amplitude-gain-bandwidth product by incorporating impedance matching elements between the active Josephson-circuit and the external feedlines has been generally successful [42, 43].

However, applying similar techniques to extend the dynamical bandwidth of JMs is quite challenging for two reasons. First, unlike the other Josephson parametric devices [42, 43, 46–48], which are degenerate, i.e., have a single differential mode and a single physical port, the JM, in contrast, is a nondegnerate device that has two distinct differential modes and two separate physical ports. Second, unlike the other JJ-based or SQUID-based devices, which have two nodes, one of which can be shorted to ground, the JRM at the center of the JM has four main nodes, none of which can be grounded without nullifying its three-wave mixing functionality.

JM design	g_0	g_1	g_2	g_3	g_4	g_5
JM_3	1	0.76	1.031	1.09	0.34	1.1055
JM_4	1	0.78	1.1	0.75	0.45	0.93

TABLE III. Prototype coefficients used in the design of JM₃ and JM₄. The prototype values are a variation on the Chebyshev coefficients of Eq. (C10), set by optimizing the simulated response of the designs in ADS at $\Phi_e = 0.6\Phi_0$.

Owing to the symmetrical structure of the JRM, we design matching networks that are mirrored across the symmetry axes of its differential modes a and b as shown in Fig. 8. Observe that for the differential mode a (b), the symmetry axis passes through a virtual ground of the shunt capacitor C_a (C_b) and the JRM. This yields $L_a = L_b = L_{out} + L_{\rm JRM}/2$ for each circuit along the symmetry axis. Furthermore, to make the symmetry and virtual ground aspects more explicit, we substitute in Fig. 8 the single shunt capacitors implemented across the JRM, i.e., C_a and C_b , with their equivalents in the form of two fictitious capacitors in series having double the capacitance, i.e., $2C_a$ and $2C_b$, respectively. Also, in this case L_J in Eq. (A4) is replaced by $L_J/2$.

Note that such modifications turn each half of the circuit (terminated by the virtual ground) into the standard circuit form discussed in Ref. [41], which can be used to design matching networks that bridge between a parametrically-modulated nonlinear inductor and the respective external ports.

In this work as shown in Fig. 8, we design the impedance-matched JMs using the coupled-mode method and implement them using lumped-element parallel LC resonators that are coupled by admittance inverters. In particular, we apply a 4-pole Chebyshev prototype for the amplifier and converter designs, whose $i^{\rm th}$

coefficient is denoted g_i , with the first g_0 corresponding to the pumped JRM and the last g_5 to the external load. The value of these coefficients, tailored for a certain response such as gain and ripple, can be calculated or found in numerous microwave-design references [41, 57, 58].

For a given frequency bandwidth $\Delta \omega_k/2\pi$ of mode $k \in \{a, b\}$, the corresponding fractional bandwidth is given by $w_k = \Delta \omega_k/\omega_k$, where ω_k is the angular resonance frequency of mode k. The values $J_{ij,k}$ of the admittance inverters are calculated using

$$J_{ij,k} = \frac{w_k}{\sqrt{g_i g_j Z_{i,k} Z_{j,k}}},\tag{C1}$$

where $i = 1, 2, 3, j = i + 1, Z_{i,k}(Z_{j,k})$ is the impedance of the $i^{\text{th}}(j^{\text{th}})$ LC resonator.

For the last admittance inverter preceding the impedance of the external feedline, i.e., $Z_{5,k} = Z_0$, we have

$$J_{45,k} = \sqrt{\frac{w_k}{g_4 g_5 Z_{4,k} Z_{5,k}}}. (C2)$$

The capacitors of the admittance inverters are given by

$$C_{ij,k} = \frac{J_{ij,k}}{\omega_k},\tag{C3}$$

where $\omega_k/2\pi$ corresponds to the center frequency of the filter on each side of the device.

The inductance $L_{i,k}$ of resonator i > 1 of mode k with impedance $Z_{i,k}$ is calculated using

$$L_{i,k} = \frac{Z_{i,k}}{\omega_k},\tag{C4}$$

where $Z_{i,k}$ (i=2,3,4) are degrees of freedom of the design, which are mainly constrained by values that can be conveniently fabricated. For simplicity, we set $Z_{2,k}=50$ Ohm and $Z_{3,k}=\sqrt{Z_{2,k}Z_{4,k}}$. Whereas, $Z_{1,k}$ is set by our choices for L_k and ω_k since $C'_{1,k}=1/\left(\omega_k^2L_k\right)$ and $Z_{1,k}=\sqrt{L_k/C'_{1,k}}$. Lastly, to eliminate the admittance inverters between the final shunt LC resonator and feedline, we set $Z_{4,k}=w_kZ_{5,k}/\left(g_4g_5\right)$.

The shunt capacitance $C_{i,k}$ of resonator $i \geq 1$ of mode k with impedance $Z_{i,k}$ is calculated using the relations

$$C_{1,k} = C'_{1,k} - C_{12,k} = 2C_k,$$
 (C5)

$$C_{2,k} = C'_{2,k} - C_{12,k} - C_{23,k},$$
 (C6)

$$C_{3,k} = C'_{3,k} - C_{23,k} - C_{34,k},$$
 (C7)

$$C_{4,k} = C'_{4,k} - C_{34,k},$$
 (C8)

where the bare capacitances $C'_{i,k}$ for the LC sections i = 2, 3, 4 read

$$C'_{i,k} = \frac{1}{\omega_k Z_{i,k}}. (C9)$$

For our coupled-mode JM amplifier (converter) design, we use a 4-pole Chebyshev prototype with 20 dB (-20 dB) of gain (reflection) and 1 dB of ripple, whose initial values are found in Ref. [41]

$$\{g_0, ..., g_5\} = \{1.0, 0.7629, 1.031, 1.1032, 0.3999, 1.1055\}.$$
(C10)

However, we set the final values for g_i by simulating each coupled-mode lumped-element JM circuit using harmonic-balance in Keysight ADS and tweaking their values based on the simulated response. The modified design coefficients for the amplifier and transducer are listed in Table III.

As to the fractional bandwidths w_k , we set them using the so-called "decrement relation" given by [41]

$$Q = \frac{|R_k|}{Z_{1,k}} = \frac{g_0 g_1}{w_k},\tag{C11}$$

where $|R_k|$ is an effective real resistance of the active component (i.e., JRM) at the desired working point and Q is the quality factor of the resonated load, which corresponds to the parallel lumped LC resonator with impedance $Z_{1,k}$ shunting the resistor. Using Eq. (C11), we obtain

$$w_k = g_0 g_1 \frac{Z_{1,k}}{|R_k|}. (C12)$$

Similar to the coefficients g_i , we optimize the value of $|R_k|$ based on the microwave simulation results of the device. In both the amplification and conversion cases, we set $|R_a| = 15$ Ohm and $|R_b| = 30$ Ohm.

To derive the scattering parameters of the device, we first calculate the total cascaded ABCD matrix of the whole device, which is obtained by multiplying the transmission ABCD (**T**) matrices of the various sections of the circuit denoted \mathbf{T}_i as shown in Fig. 8

$$\mathbf{T}_{\text{total}} = \prod_{i=1}^{15} \mathbf{T}_i, \tag{C13}$$

where the matrices \mathbf{T}_{i} ($i \neq 8$) representing the coupling capacitors and LC resonators are given in Fig. 9, while $\mathbf{T}_{8} = \mathbf{T}_{JRM}$ representing the JRM is given in Fig. 3(b) for the amplifier and transducer cases.

Afterwards, we substitute the ABCD elements of $\mathbf{T}_{\text{total}}$ into Eqs. (B5)-(B8) to get the scattering parameters of the coupled-mode JM device.

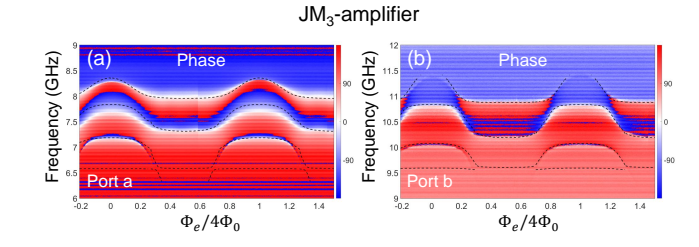


FIG. 16. (a) Phase of the reflected signal off port a of JM_3 measured as a function of frequency and normalized applied flux (Pump off). (b) same as (a) measured for port b. The dashed black curves are theoretical fits. The device parameters used in producing the fits are listed in Table IV.

2. Flux tunability and device parameters

Figure 16 (a) and (b) exhibit the reflection parameter phase measured for port a and b of JM₃ as a function of frequency and applied external flux. We fit the resonance frequencies of the coupled modes of the device using the theoretical model outlined in Appendix C.1. The calculated fits are plotted on top of the data using dashed black curves. The circuit parameters employed in the fits are listed in Table IV. Note that since the flux tunability data is taken with no pump $I_p = 0$, substituting $\alpha = 0$ in the JM model of Appendix C.1 leads to divergence in \mathbf{T}_{JRM} (i.e., \mathbf{T}_8). To circumvent that, we assume a very small non-zero pump in the calculation (e.g., $\alpha = 0.001$).

Figure 17 (a) and (b) exhibit the reflection parameter phase measured for port a and b of JM_4 as a function of frequency and applied external flux. Similarly, we fit the resonance frequencies of the coupled modes of the device using the theoretical model outlined in Appendix C.1. The circuit parameters employed in the fits are listed in Table V.

It is important to point out that due to the large number of design parameters associated with $JM_{3,4}$, we impose three restrictions in the fitting process, (1) we set the parameter values associated with the JRM and L_{out} to be identical (based on the best fits applicable to both devices), (2) we assume that for each port (i.e., A and B) the lumped-element matching networks realized along the arm J_1 and K_1 are identical to those along J_2 and K_2 (as defined in Fig. 1 (c)), and (3) we limit the possible variation of the various parameter values to less than $\pm 10\%$ compared to the respective ideal original design.

Appendix D: JM simulation model

As stated in the main text, the simulation results are obtained using the harmonic-balance tool in Keysight ADS (2023 version). The circuit schematic applied in the simulation is identical to the lumped-element circuit displayed in Fig. 1(a) in combination with the trivial

	$ m JM_3$ circuit parameters											
I_0	$2.5~\mu\mathrm{A}$	$L_{2,a}$ 1.17 nH	$C_{2,a} = 0.13 \text{ p}$	oF $L_{2,b}$ 0.8 n	H $C_{2,b}$ 0.177 pF							
$ L_{J0} $	$132~\mathrm{pH}$	$L_{3,a}$ 0.597 nH	$C_{3,a} = 0.573$	pF $\left L_{3,b}\right $ 0.333 i	$_{ m nH} \left C_{3,b} \left 0.575 { m pF} \right \right $							
$\parallel L_s$	10 pH	$L_{4,a}$ 0.302 nH	$I \mid C_{4,a} = 1.585$	pF $ L_{4,b} $ 0.132 i	$nH \mid C_{4,b} \mid 1.751 \text{ pF} \mid$							
$\ L_{in}\ $	$30~\mathrm{pH}$		$C_{12,a} \ 0.215$	pF	$C_{12,b} \ 0.101 \ \mathrm{pF}$							
$\ L_{out}\ $	9 pH		$C_{23,a} \ 0.052$	pF	$C_{23,b}$ 0.03 pF							
C_a	$6.276~\mathrm{pF}$		$C_{34,a} \ 0.171$	pF	$C_{34,b} \ 0.124 \ \mathrm{pF}$							
C_b	$3.217~\mathrm{pF}$											

TABLE IV. Circuit parameters of JM_3 device obtained from the theory fits of the measured frequency response versus applied flux (Fig. 16).

	$ m JM_4$ circuit parameters									
I_0	$2.5~\mu\mathrm{A}$	$L_{2,a}$	1.131	nΗ	$C_{2,a}$	0.12 pF	$L_{2,b}$	0.804 nH	$C_{2,b}$	0.171 pF
L_{J0}	$132~\mathrm{pH}$	$L_{3,a}$	0.575	nH	$C_{3,a}$	$0.582~\mathrm{pF}$	$L_{3,b}$	$0.343~\mathrm{nH}$	$C_{3,b}$	0.561 pF
L_s	10 pH	$L_{4,a}$	0.292	nH	$C_{4,a}$	$1.517~\mathrm{pF}$	$L_{4,b}$	$0.146~\mathrm{nH}$	$C_{4,b}$	1.616 pF
L_{in}	$30~\mathrm{pH}$				$C_{12,a}$	$0.239~\mathrm{pF}$			$C_{12,b}$	0.106 pF
L_{out}	$9~\mathrm{pH}$				$C_{23,a}$	$0.073~\mathrm{pF}$			$C_{23,b}$	0.04 pF
C_a	$6.287~\mathrm{pF}$				$C_{34,a}$	$0.219~\mathrm{pF}$			$C_{34,b}$	0.142 pF
C_b	$3.219~\mathrm{pF}$									

TABLE V. Circuit parameters of JM₄ device obtained from the theory fits of the measured frequency response versus applied flux (Fig. 17).

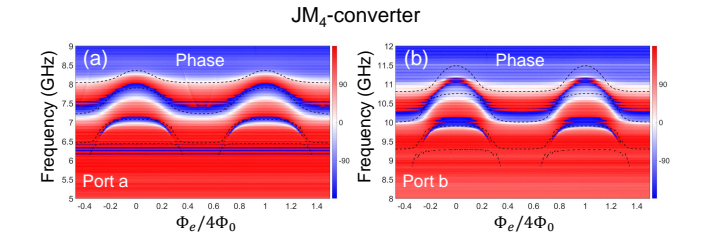


FIG. 17. (a) Phase of the reflected signal off port a of $\rm JM_4$ measured as a function of frequency and normalized applied flux (Pump off). (b) same as (a) measured for port b. The dashed black curves are theoretical fits. The device parameters used in producing the fits are listed in Table V.

matching network shown in (b) in the case of JM_1 and JM_2 or the coupled-mode matching network exhibited in (c), in the case of JM_3 and JM_4 . Also, similar to the experimental setup shown in Fig. 18, we excite ports a and b of the JM differentially using ideal 180 degree hybrids.

The JJs of the JRM are modeled using the JJ3 circuit element. To mimic the effect of flux biasing in the loop, we apply a circulating current in the JRM by connecting an ideal dc-current source shunted by a large capacitor (1 F) in series with each JJ. The current of the dc source is set by the corresponding superconducting current flowing in the outer loop, I_{ϕ} given by Eq. (A5), whereas the large shunt capacitor is added to act like an open at dc (across the current source) and a short at microwave frequencies.

It is important to point out that the harmonic-balance

simulation we use suffers from convergence limitations, which prevent us from fully simulating the JM circuit at any desired working point. In particular, the simulation breaks down when applying magnetic fluxes beyond $0.75-0.8\Phi_0$, or when the input signal power exceeds the saturation power by a few dBm, or when the applied pump power becomes "appreciable", depending on the circuit, pump frequency, and applied flux. Thus, due to these convergence limitations, our optimization of the JM design parameters is mainly done by simulating their operation near $0.6\Phi_0$.

In Tables VI, VII, we list the external fluxes and pump frequencies, which we employ to obtain the various measurement results, calculated responses, and simulated curves exhibited in the main text. The flux and pump parameters employed in the calculation and simulation were generally treated as degrees of freedom, whose values are chosen based on the resultant agreement between the measured and generated response with respect to their frequency range, shape, and magnitude.

Appendix E: Setup

A schematic diagram of the fridge setup used in the measurement of the JM devices is shown in Fig. 18. It includes two input and output lines for probing ports a and b of the JMs. As seen in the diagram the input and output lines are joined via routers that separate the incoming and outgoing microwave signals reflecting off the JM ports. In one experimental version, the signal

	JM ₁ results							$ m JM_2$ 1	esults	
Fig.	4(c)(d)	4(c)(d) 4(i)(j) 4(k)(l) 4(p)(q) 5(a)(b) 5(c)(d)						6(g)(h)	6(i)(j)	6(m)(n)
Φ_e/Φ_0	1.45	1.24	0.7	0.7	1.6	1.5	1.06	0.93	1.2	0.8
f_p (GHz)	17.381	17.484	17.5	18	16.506	16.3	2.9	2.996	2.8	2.8

TABLE VI. External flux and pump frequency applied in the measurement, calculation, and simulation of JM₁ and JM₂.

	J	M_3 result	ts	$ m JM_4$ results				
Fig.	10(a)(b)	10(c)(d)	10(g)(h)	12(a)(b)	12(c)(d)	12(g)(h)	13(a)(b)	
Φ_e/Φ_0	0.776	1	0.75	0.45	0.95	0.75	0.4	
f_p (GHz)	18.418	18.2	18.41	3.12	3	3.01	2.86	

TABLE VII. External flux and pump frequency applied in the measurement, calculation, and simulation of JM₃ and JM₄.

router is realized using a three-port magnetic circulator, while in another it is implemented using a 20-dB directional coupler (whose "isolated" port is terminated by a 50 Ohm). We use the former, denoted configuration 1, to measure JM_1 and JM_2 , and the latter, denoted configuration 2, to measure JM_3 and JM_4 . Due to these changes in the setup, the two groups of JM devices are characterized in two separate cooldowns. To balance the total attenuation of the input lines, we incorporate 20 dB attenuators at the 4 K stage when using the circulators. These added attenuators compensate for the attenuation of 20 dB introduced by the directional couplers in configuration 2.

As seen in the setup diagram, to excite the differential modes a (b) of the JMs, we connect their ports A_1 and A_2 (B_1 and B_2) to commercial wideband 180 degree hybrids (Krytar 6 – 20 GHz) and probe their response through the delta (Δ) ports of the couplers, while terminating the sum (Σ) ports of the hybrids by 50 Ohm cold loads.

Furthermore, to enable testing of more than one JM device per cooldown, we use two 6-way Radiall switches, whose common ports connect to the routers assigned for measuring ports a and b of the JMs. In addition to the JM devices under test, we allocate entries on the switches for calibrating the reflection parameters in-situ, which we connect to coax cables and hybrids that are nominally identical to the ones used in the JM measurement, terminated instead by an open or a short.

Due to necessary spacings and mounting constraints of the various components at the base temperature stage, relatively long coaxial lines 0.5-0.6 m are used to connect between the different components. Examples of such constraints include housing the JM devices deep inside a cryoperm magnetic shield and mounting the JM devices away from the magnetic components, i.e., isolators and circulators. However, incorporating such relatively long coaxial lines between the intermediate parts at the base stage gives rise to unwanted ripples in the measured frequency response of the JMs, originating from standing waves in the lines due to mismatches in the impedance of the various ports, especially those belonging to the routers and samples (see Appendix G for more details).

The pump drives are fed to the JMs though separate input lines, which include wideband 20 dB directional couplers at the base stage. The couplers attenuate the pump tones that drive the JMs by directing a large portion of their powers towards the 4 K stage where they get dissipated in 50 Ohm terminations.

Appendix F: Scattering parameters of resonant-mode JMs operated in conversion

For completeness, we present here the reflection and transmission parameters used in producing the theoretical results shown in Fig. 7 and fits in Fig. 15 (b), (d). For resonant-mode JMs operated in conversion, the transmission parameter can be written as [28]

$$S_{ab} = \frac{2i\rho e^{-i\phi_p}}{\chi_a^{-1}\chi_b^{-1} + \rho^2},\tag{F1}$$

$$S_{ba} = \frac{2i\rho e^{i\phi_p}}{\chi_a^{-1}\chi_b^{-1} + \rho^2},\tag{F2}$$

where $\rho \geq 0$ is a dimensionless parameter representing the pump amplitude and $\chi's$ are the bare response functions of modes a and b, whose inverses depend linearly on the signal and idler frequencies f_1 and f_2 , respectively:

$$\chi_a^{-1}[\omega_1] = 1 - 2i \frac{\omega_1 - \omega_a}{\gamma_a},$$

$$\chi_b^{-1}[\omega_2] = 1 - 2i \frac{\omega_2 - \omega_b}{\gamma_b},$$
 (F3)

where $\omega_1 = 2\pi f_1$, $\omega_a = 2\pi f_a$ and the applied pump angular frequency is given by $\omega_p = \omega_b - \omega_a = \omega_2 - \omega_1$, where $\omega_b = 2\pi f_b$ and $\omega_2 = 2\pi f_2$.

Similarly, the JM reflection parameters at ports 'a' and 'b', can be written as

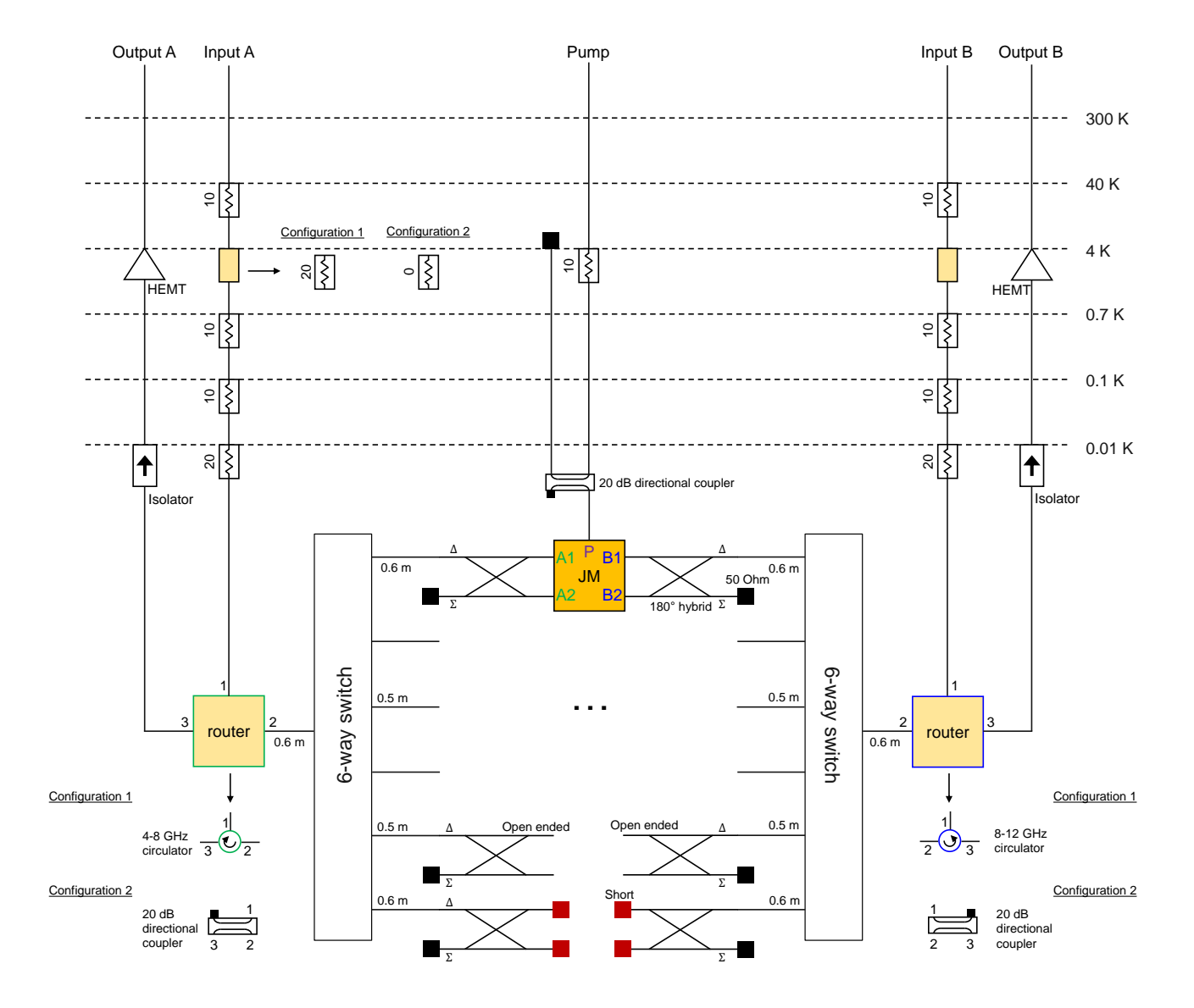


FIG. 18. Experimental setup used in the characterization and measurement of the different JMs. Ports a and b of the tested JM are connected to Krytar 180 degree hybrids used for exciting the differential modes a and b (the input and output signals pass through the delta port). The pump drives are directly fed to the JM devices and carried by separate input lines. Two 6-way switches are used to switch between JMs of different designs and 180 degree hybrids that are terminated by an open or a short are used for calibration measurements. JM₁ and JM₂ are measured using configuration 1, in which the switch assigned to port a (b) of the JMs is connected through a circulator to the input and output lines of mode a (b), and a 20 dB attenuator is included in the input line A (B) at the 4 K stage. Whereas, JM₃ and JM₄ are measured using configuration 2, in which the switch assigned to port a (b) of the JMs is connected through a 20 dB directional coupler to the input and output lines of mode a (b), and no attenuator is included in the input line A (B) at the 4 K stage.

Appendix G: Effect of interference and multiple reflections on the measured response

$$S_{aa}[\omega_1] = \frac{\chi_a^{-1*} \chi_b^{-1} - \rho^2}{\chi_a^{-1} \chi_b^{-1} + \rho^2},$$
 (F4)
$$S_{bb}[\omega_2] = \frac{\chi_a^{-1} \chi_b^{-1*} - \rho^2}{\chi_a^{-1} \chi_b^{-1} + \rho^2}.$$
 (F5)

$$S_{bb}[\omega_2] = \frac{\chi_a^{-1} \chi_b^{-1*} - \rho^2}{\chi_a^{-1} \chi_b^{-1} + \rho^2}.$$
 (F5)

Most ripples seen in the reflection measurements of the JM devices, especially those with large bandwidths, originate from interference effects caused by multiple reflections in the experimental setup; primarily between the JM ports and the corresponding signal "routers" (i.e., circulators or directional couplers shown in Fig. 18), which

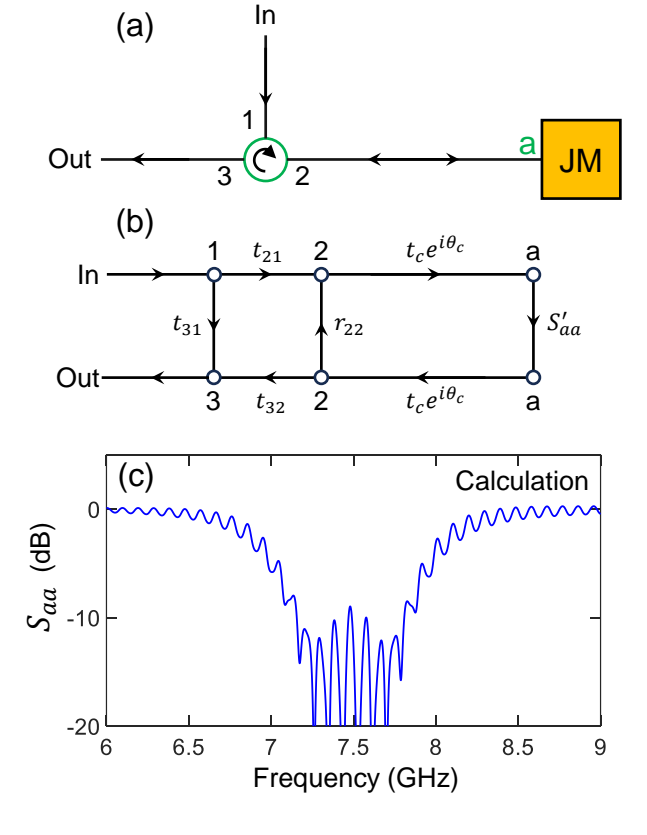


FIG. 19. (a) Simplified diagram of the reflection measurement setup. (b) The corresponding signal flow graph. (c) Normalized reflection response calculated for the working point of JM₂ exhibited in Fig. 6(g). In the calculation, we model the effect of reflections and wave interference taking place in the setup based on the signal flow graph shown in (b) (see text for more details). The parameter values employed in the calculation are, $t = t_{21} = t_{32} = t_c = 0.95$, $t_{31} = 0.1$, $r_{22} = 0.17$, $l_c = 1.1$ m, and $\varepsilon = 2.1$.

are connected via coaxial cable lines with lengths of about $1.1-1.2~\mathrm{m}.$

To demonstrate the pronounced ripple effect generated in the reflection measurement setup, we use a simple interference model depicted in Fig. 19. In panel (a) we sketch a simplified diagram of the reflection measurement setup; consisting of an input line connected to port 1 of a three-port circulator, a JM device whose port a is connected to port 2 of the circulator via a relatively long coaxial cable, and an output line connected to port 3 of the circulator. In panel (b), we draw the corresponding signal flow graph for the simplified reflection setup presented in (a). Next to the arrows indicating the possible paths taken by the signals propagating between the input and output lines, we list the reflection or transmission amplitudes associated with the different path sections. In the graph, t_{21} and t_{32} represent the transmission amplitudes through the circulator from port 1 to 2 and 2 to 3, which are aligned with its circulation direction. In

contrast, t_{31} represents the transmission amplitude from port 1 to 3 of the circulator, which corresponds to transmission in the opposite direction. Similarly, t_c and θ_c represent the transmission amplitude and accumulated phase through the coaxial lines connecting the circulator and the JM port. While r_{22} and S'_{aa} represent the amplitude of the reflection off port 2 of the circulator and port a of the JM, respectively.

By inspection, we can write down the effective reflection parameter amplitude S_{aa} measured in the experiment

$$S_{aa} = t_{31} + \frac{t_{32}t_{21}t_c^2e^{2i\theta_c}S'_{aa}}{1 - r_{22}S'_{aa}t_c^2e^{2i\theta_c}},$$
 (G1)

where $\theta_c = 2\pi f_1 \sqrt{\varepsilon} l_c/c$, c is the speed of light in vacuum, l_c is the length of the coaxial cables, and ε is the relative permittivity constant of the dielectric material in the cables. Although Eq. (G1) is derived for port a of the JM, a similar relation can be obtained for reflections off port b.

For simplicity, we assume that all transmission and reflection parameter amplitudes that are not related to the JM, i.e., t_{31} , t_{32} , t_{21} , t_c , r_{22} are real and independent of frequency. Whereas, S'_{aa} is calculated for each input frequency using Eq. (B5) or Eq. (F4) depending on the particular case.

As an example, we apply Eq. (G1) to the working point of JM₂ presented in Fig. 6(g). Since the pump-on reflection measurement shown in Fig. 6(g) is normalized by the pump off measurement, we plot in Fig. 19(c) the calculated normalized response $|S_{aa}|^2 = |S_{aa}^{\rm on}/S_{aa}^{\rm off}|^2$, where both $S_{aa}^{\rm on}$ and $S_{aa}^{\rm off}$ are calculated using Eq. (G1) (which correspond to different S_{aa}'). In the $S_{aa}^{\rm off}$ case, we employ Eq. (F4) to calculate S_{aa}' for $\rho=0$, $\gamma_a/2\pi=400$ MHz, and $\gamma_b/2\pi=900$ MHz, whereas in the $S_{aa}^{\rm on}$ case, we employ Eq. (B5) (whose result is plotted in Fig. 6(i)). In the calculation we assume that the JM is lossless and that the circulator has an insertion loss of about -0.45 dB in the forward direction, power reflection of about -15 dB, and power isolation of 20 dB. We also assume that the coaxial cables have a similar insertion loss in each direction -0.45 dB.

As seen in Fig. 19(c), the ripples in the calculated response can be as significant as the ones observed in the measured data especially in band. We also note that the average ripple separation in frequency is about 90 MHz in the calculation compared to about 80 in the experiment. While understandably the simple model presented in this section cannot produce every feature in the data, it generally explains most of the ripples and dips seen in the reflection curves.

Appendix H: Added noise in amplification

To show that the nondegenerate Josephson amplifiers, i.e., JM_1 and JM_3 , operate near the quantum limit, we measure the improvement in the signal-to-noise ratio of

the output chain of port k, which is given by $G/G_{N,k}$, where G is the power gain of the JM and $G_{N,k}$ is the output noise ratio (or noise rise) corresponding to the JM being on versus off

$$G_{N,k} = \frac{T_{N,k} + GT_{Q,k}n_{\text{vac}} + (G-1)T_{Q,k}n_{\text{add}}}{T_{N,k} + T_{Q,k}},$$
 (H1)

where $T_{Q,k} = \hbar \omega_k / k_B$ is the equivalent temperature of a

mode k photon, $T_{N,k}$ is the effective noise temperature of the output chain for mode k in the absence of the JM, $n_{\text{vac}} = 1/2$ is input vacuum noise, and n_{add} is the number of noise equivalent input photons added by the JM.

Using Eq. (H1), the signal-to-noise ratio improvement due to the JM reads

$$\frac{G}{G_{N,k}} = \frac{T_{N,k} + T_{Q,k}}{T_{N,k}/G + T_{Q,k} \left[n_{\text{vac}} + n_{\text{add}} \left(G - 1 \right) / G \right]}. \quad (\text{H2})$$

- [1] B. Yurke, L. R. Corruccini, P. G. Kaminsky, and L. W. Rupp, A. D. Smith, A. H. Silver, R. W. Simon, and E. A. Whittaker, Observation of parametric amplification and deamplification in a Josephson parametric amplifier, Phys. Rev. A 39, 2519 (1989).
- [2] C. M. Caves, Quantum limits on noise in linear amplifiers, Phys. Rev. D 26, 1817 (1982).
- [3] A. A. Clerk, M. H. Devoret, S. M. Girvin, F. Marquardt, and R. J. Schoelkopf, *Introduction to quantum noise*, measurement, and amplification, Rev. Mod. Phys. 82, 1155 (2010).
- [4] M. H. Devoret and R. J. Schoelkopf, Superconducting circuits for quantum information: An Outlook, Science 339, 1169 (2013).
- [5] Jay M. Gambetta, Jerry M. Chow, and Matthias Steffen, Building logical qubits in a superconducting quantum computing system, npj Quantum Inf. 3, 2 (2017).
- [6] Jay Gambetta, Alexandre Blais, M. Boissonneault, A. A. Houck, D. I. Schuster, and S. M. Girvin, Quantum trajectory approach to circuit QED: Quantum jumps and the Zeno effect, Phys. Rev. A 77, 012112 (2008).
- [7] R. Vijay, D. H. Slichter, and I. Siddiqi, Observation of quantum jumps in a superconducting artificial atom, Phys. Rev. Lett. 106, 110502 (2011).
- [8] R. Vijay, C. Macklin, D. H. Slichter1, S. J. Weber, K. W. Murch, R. Naik, A. N. Korotkov, and I. Siddiqi, Stabilizing Rabi oscillations in a superconducting qubit using quantum feedback, Nature 490, 77 (2012).
- [9] M. Hatridge, S. Shankar, M. Mirrahimi, F. Schackert, K. Geerlings, T. Brecht, K. M. Sliwa, B. Abdo, L. Frunzio, S. M. Girvin, R. J. Schoelkopf, and M. H. Devoret, Quantum back-action of an individual variable-strength measurement, Science 339, 178 (2013).
- [10] Nissim Ofek, Andrei Petrenko, Reinier Heeres, Philip Reinhold, Zaki Leghtas, Brian Vlastakis, Yehan Liu,, Luigi Frunzio, S. M. Girvin, L. Jiang, Mazyar Mirrahimi, M. H. Devoret, and R. J. Schoelkopf Extending the lifetime of a quantum bit with error correction in superconducting circuits, Nature 536, 441 (2016).
- [11] Baleegh Abdo, Katrina Sliwa, Flavius Schackert, Nicolas Bergeal, Michael Hatridge, Luigi Frunzio, A. Douglas Stone, and Michel Devoret Full Coherent Frequency Conversion between Two Propagating Microwave Modes, Phys. Rev. Lett. 110, 173902 (2013).
- [12] Benjamin J. Chapman, Stijn J. de Graaf, Sophia H. Xue, Yaxing Zhang, James Teoh, Jacob C. Curtis, Takahiro Tsunoda, Alec Eickbusch, Alexander P. Read, Akshay Koottandavida, Shantanu O. Mundhada, Luigi Frun-

- zio, M.H. Devoret, S.M. Girvin, and R.J. Schoelkopf, *High-On-Off-Ratio Beam-Splitter Interaction for Gates on Bosonically Encoded Qubits*, PRX Quantum 4, 020355 (2023).
- [13] E. Flurin, N. Roch, J. D. Pillet, F. Mallet, and B. Huard, Superconducting quantum node for entanglement and storage of microwave radiation, Phys. Rev. Lett. 114, 090503 (2015).
- [14] A. J. Sirois, M. A. Castellanos-Beltran, M. P. DeFeo, L. Ranzani, F. Lecocq, R. W. Simmonds, J. D. Teufel, and J. Aumentado, Coherent-state storage and retrieval between superconducting cavities using parametric frequency conversion, Appl. Phys. Lett. 106, 172603 (2015).
- [15] Yao Lu, Aniket Maiti, John W. O. Garmon, Suhas Ganjam, Yaxing Zhang, Jahan Claes, Luigi Frunzio, Steven M. Girvin, andRobert J. Schoelkopf, High-fidelity parametric beamsplitting with a parity-protected converter, Nat. Commun. 14, 5767 (2023).
- [16] L. Ranzani, and J. Aumentado, Circulators at the quantum limit: Recent realizations of quantum-limited superconducting circulators and related approaches, IEEE Micro. Mag. 20, 112-122 (2019).
- [17] Leonardo Ranzani, Shlomi Kotler, Adam J. Sirois, Michael P. DeFeo, Manuel Castellanos-Beltran, Katarina Cicak, Leila R. Vale, and José Aumentado, Wideband Isolation by Frequency Conversion in a Josephson-Junction Transmission Line, Phys. Rev. Applied 8, 054035 (2017).
- [18] E. I. Rosenthal, B. J. Chapman, A. P. Higginbotham, J. Kerckhoff, and K. W. Lehnert, *Breaking Lorentz reci*procity with frequency conversion and delay, Phys. Rev. Lett. 119, 147703 (2017).
- [19] K. M. Sliwa, M. Hatridge, A. Narla, S. Shankar, L. Frunzio, R. J. Schoelkopf, and M. H. Devoret, *Reconfigurable Josephson circulator/directional amplifier*, Phys. Rev. X 5, 041020 (2015).
- [20] Randy Kwende, Theodore White, Ofer Naaman, Josephson parametric circulator with same-frequency signal ports, 200 MHz bandwidth, and high dynamic range, Appl. Phys. Lett. 122, 224001 (2023).
- [21] Baleegh Abdo, Nicholas T. Bronn, Oblesh Jinka, Salvatore Olivadese, Antonio D. Córcoles, Vivekananda P. Adiga, Markus Brink, Russell E. Lake, Xian Wu, David P. Pappas, and Jerry M. Chow, Active protection of a superconducting qubit with an interferometric Josephson isolator, Nat. Commun. 10, 3154 (2019).
- [22] Baleegh Abdo, Oblesh Jinka, Nicholas T. Bronn, Salvatore Olivadese, and Markus Brink, High-Fidelity Qubit

- Readout Using Interferometric Directional Josephson Devices, PRX Quantum 2, 040360 (2021).
- [23] M. Hatridge, R. Vijay, D. H. Slichter, John Clarke, and I. Siddiqi, Dispersive magnetometry with a quantum limited SQUID parametric amplifier, Phys. Rev. B 83, 134501, (2011).
- [24] N. E. Frattini, V. V. Sivak, A. Lingenfelter, S. Shankar, and M. H. Devoret, Optimizing the Nonlinearity and Dissipation of a SNAIL Parametric Amplifier for Dynamic Range, Phys. Rev. Applied 10, 054020 (2018).
- [25] N. Bergeal, F. Schackert, M. Metcalfe, R. Vijay, V. E. Manucharyan, L. Frunzio, D. E. Prober, R. J. Schoelkopf, S. M. Girvin, and M. H. Devoret, *Phase-preserving amplification near the quantum limit with a Josephson ring modulator*, Nature 465, 64 (2010).
- [26] Baleegh Abdo, Flavius Schackert, Michael Hatridge, Chad Rigetti, and Michel Devoret, Josephson amplifier for qubit readout, Appl. Phys. Lett. 99, 162506 (2011).
- [27] N. Bergeal, R. Vijay, V. E. Manucharyan, I. Siddiqi, R. J. Schoelkopf, S. M. Girvin, and M. H. Devoret, Analog information processing at the quantum limit with a Josephson ring modulator, Nature Phys. 6, 296 (2010).
- [28] Baleegh Abdo, Archana Kamal, and Michel Devoret, Nondegenerate three-wave mixing with the Josephson ring modulator, Phys. Rev. B 87, 014508 (2013).
- [29] Baleegh Abdo, Jose M. Chavez-Garcia, Markus Brink, George Keefe, and Jerry M. Chow, Time-multiplexed amplification in a hybrid-less and coil-less Josephson parametric converter, Appl. Phys. Lett. 110, 082601 (2017).
- [30] C. Macklin, K. O'Brien, D. Hover, M. E. Schwartz, V. Bolkhovsky, X. Zhang, W. D. Oliver, and I. Siddiqi, A near-quantum-limited Josephson traveling-wave parametric amplifier, Science 350, 307-310 (2015).
- [31] Jennifer Wang, Kaidong Peng, Jeffrey M. Knecht, Gregory D. Cunningham, Andres E. Lombo, Alec Yen, Daniela A. Zaidenberg, Michael Gingras, Bethany M. Niedzielski, Hannah Stickler, Katrina Sliwa, Kyle Serniak, Mollie E. Schwartz, William D. Oliver, Kevin P. O'Brien, High-Efficiency, Low-Loss Floquet-mode Traveling Wave Parametric Amplifier, arXiv:2503.11812 (2025).
- [32] C. W. Sandbo Chang, Arjan F. Van Loo, Chih-Chiao Hung, Yu Zhou, Christian Gnandt, Shuhei Tamate, Yasunobu Nakamura, Josephson traveling-wave parametric amplifier based on low-intrinsic-loss coplanar lumpedelement waveguide, arXiv:2503.07559 (2025).
- [33] T. C. White, J. Y. Mutus, I.-C. Hoi, R. Barends, B. Campbell, Yu Chen, Z. Chen, B. Chiaro, A. Dunsworth, E. Jeffrey, J. Kelly, A. Megrant, C. Neill, P. J. J. O'Malley, P. Roushan, D. Sank, A. Vainsencher, J. Wenner, S. Chaudhuri, J. Gao, John M. Martinis Traveling wave parametric amplifier with Josephson junctions using minimal resonator phase matching, Appl. Phys. Lett. 106, 242601 (2015).
- [34] Martina Esposito, Arpit Ranadive, Luca Planat, Sébastien Leger, Dorian Fraudet, Vincent Jouanny, Olivier Buisson, Wiebke Guichard, Cécile Naud, José Aumentado, Florent Lecocq, and Nicolas Roch, Observation of two-mode squeezing in a traveling wave parametric amplifier, Phys. Rev. Lett. 128, 153603 (2022).
- [35] M.R. Perelshtein, K.V. Petrovnin, V. Vesterinen, S. Hamedani Raja, I. Lilja, M. Will, A. Savin, S. Simbierowicz, R.N. Jabdaraghi, J.S. Lehtinen, L. Grönberg, J. Hassel, M.P. Prunnila, J. Govenius, G.S. Paraoanu,

- and P.J. Hakonen, Broadband continuous variable entanglement generation using Kerr-free Josephson metamaterial, Phys. Rev. Appl. 18, 024063 (2022).
- [36] A. Zorin, Josephson Traveling-Wave Parametric Amplifier with Three-Wave Mixing, Phys. Rev. Appl. 6, 034006 (2016).
- [37] Victor Gaydamachenko, Christoph Kissling, Lukas Grünhaupt, An rf-SQUID-based traveling-wave parametric amplifier with -84 dBm input saturation power across more than one octave bandwidth, arXiv:2503.02489v1 (2025).
- [38] Kevin O'Brien, Chris Macklin, Irfan Siddiqi, and Xiang Zhang, Resonant Phase Matching of Josephson Junction Traveling Wave Parametric Amplifiers, Phys. Rev. Lett. 113, 157001 (2014).
- [39] Theodore White et al., Readout of a quantum processor with high dynamic range Josephson parametric amplifiers, Appl. Phys. Lett. 122, 014001 (2023).
- [40] Kevin O'Brien, Nonlinear Light-Matter Interactions in Metamaterials, PhD Thesis (2016).
- [41] O. Naaman and J. Aumentado, Synthesis of parametrically coupled networks, PRX Quantum 3, 020201 (2022).
- [42] Tanay Roy, Suman Kundu, Madhavi Chand, A. M. Vadiraj, A. Ranadive, N. Nehra, Meghan P. Patankar, J. Aumentado, A. A. Clerk, and R. Vijay, Broadband parametric amplification with impedance engineering: Beyond the gain-bandwidth product, Appl. Phys. Lett. 107, 262601 (2015).
- [43] J. Y. Mutus, T. C. White, R. Barends, Yu Chen, Z. Chen, B. Chiaro, A. Dunsworth, E. Jeffrey, J. Kelly, A. Megrant, C. Neill, P. J. J. O'Malley, P. Roushan, D. Sank, A. Vainsencher, J. Wenner, K. M. Sundqvist, A. N. Cleland, and John M. Martinis, Strong environmental coupling in a Josephson parametric amplifier, Appl. Phys. Lett. 104, 263513 (2014).
- [44] J. Grebel, A. Bienfait, É. Dumur, H.-S. Chang, M.-H. Chou, C. R. Conner, G. A. Peairs, R. G. Povey, Y. P. Zhong, and A. N. Cleland, Flux-pumped impedance-engineered broadband Josephson parametric amplifier, Appl. Phys. Lett. 118, 142601 (2021).
- [45] P. Duan, Z. Jia, C. Zhang, L. Du, H. Tao, X. Yang, L. Guo, Y. Chen, H. Zhang, Z. Peng, W. Kong, H.-O. Li, G. Cao, and G.-P. Guo, Broadband flux-pumped Josephson parametric amplifier with an on-chip coplanar waveguide impedance transformer, Appl. Phys. Express 14, 042011 (2021).
- [46] Bingcheng Qing, Long B. Nguyen, Xinyu Liu, Hengjiang Ren, William P. Livingston, Noah Goss, Ahmed Hajr, Trevor Chistolini, Zahra Pedramrazi, David I. Santiago, Jie Luo, and Irfan Siddiqi, Broadband coplanarwaveguide-based impedance-transformed Josephson parametric amplifier, Phys. Rev. Research 6, L012035 (2024).
- [47] Ryan Kaufman, Theodore White, Mark I. Dykman, Andrea Iorio, George Sterling, Sabrina Hong, Alex Opremcak, Andreas Bengtsson, Lara Faoro, Joseph C. Bardin, Tim Burger, Robert Gasca, and Ofer Naaman, Josephson parametric amplifier with Chebyshev gain profile and high saturation, Phys. Rev. Applied 20, 054058 (2023).
- [48] V. R. Joshi, S. Hazra, A. Z. Ding, A. Miano, W. Dai, G. Umasankar, A. Kottandavida, G. Liu, L. Frunzio, and M. H. Devoret, Lumped-element broadband SNAIL parametric amplifier with on-chip pump filter for multiplexed readout, arXiv:2505.02740v1 (2025).

- [49] G. Liu, T.-C. Chien, X. Cao, O. Lanes, E. Alpern, D. Pekker, M. Hatridge, Josephson parametric converter saturation and higher order effects, Appl. Phys. Lett. 111, 202603 (2017).
- [50] T.-C. Chien, O. Lanes, C. Liu, X. Cao, P. Lu, S. Motz, G. Liu, D. Pekker, and M. Hatridge, Multiparametric amplification and qubit measurement with a Kerr-free Josephson ring modulator, Phys. Rev. A 101, 042336 (2020).
- [51] N. Roch, E. Flurin, F. Nguyen, P. Morfin, P. Campagne-Ibarcq, M. H. Devoret, and B. Huard, Widely tunable, nondegenerate three-wave mixing microwave device operating near the quantum limit, Phys. Rev. Lett. 108, 147701 (2012).
- [52] Chenxu Liu, Tzu-Chiao Chien, Michael Hatridge, and David Pekker, Optimizing Josephson-ringmodulator-based Josephson parametric amplifiers via full Hamiltonian control, Phys. Rev. A 101, 042323 (2020).
- [53] Zheng Cui, John R. Kirtley, Yihua Wang, Philip A. Kratz, Aaron J. Rosenberg, Christopher A. Watson, Gerald W. Gibson Jr., Mark B. Ketchen, and Kathryn. A. Moler, Scanning SQUID sampler with 40-ps time resolution, Rev. Sci. Instrum. 88, 083703 (2017).
- [54] Dong Hwan Kim, Su-Yong Lee, Zaeill Kim, Taek Jeong, and Duk Y. Kim, Squeezing Limit of the Josephson Ring Modulator as a Nondegenerate Parametric Amplifier, Phys. Rev. Applied 19, 034015 (2023).
- [55] J. M. Manely and H. E. Rowe, Some general properties of nonlinear elements-part I, Proc. IRE 44, 904 (1956).
- [56] D. M. Pozar, Microwave Engineering. 3rd edn (Wiley, Hoboken, 2005).
- [57] G. L. Matthaei, A study of the optimum design of wideband parametric amplifiers and up-converters, IRE Trans. MTT 9, 23 (1961).

- [58] W. J. Getsinger, Prototypes for use in broadbanding reflection amplifiers, IEEE Trans. MTT 11, 486 (1963).
- [59] B. T. Henoch, A new method for designing wide-band parametric amplifiers, IEEE Trans. Microw. Theory Tech. 11, 62 (1963).
- [60] D. Mellor and J. Linvill, Synthesis of interstage networks of prescribed gain versus frequency slopes, IEEE Trans. Microw. Theory Tech. 23, 1013 (1975).
- [61] G. Liu, X. Cao, T.-C. Chien, C. Zhou, P. Lu, and M. Hatridge, Noise Reduction in Qubit Readout with a Two-Mode Squeezed Interferometer, Phys. Rev. Applied 18, 064092, (2022).
- [62] B. Abdo, W. Shanks, O. Jinka, J. R. Rozen, J. Orcutt, Teleportation and Entanglement Swapping of Continuous Quantum Variables of Microwave Radiation, arXiv:2501.05537 (2025).
- [63] W. K. Yam, M. Renger, S. Gandorfer, F. Fesquet, M. Handschuh, K. E. Honasoge, F. Kronowetter, Y. Nojiri, M. Partanen, M. Pfeiffer, H. van der Vliet, A. J. Matthews, J. Govenius, R. N. Jabdaraghi, M. Prunnila, A. Marx, F. Deppe, R. Gross, and K. G. Fedorov, Cryogenic microwave link for quantum local area networks, arxiv:2308.12398 (2023).
- [64] E. Flurin, N. Roch, F. Mallet, M. H. Devoret, and B. Huard, Generating entangled microwave radiation over two transmission lines, Phys. Rev. Lett. 109, 183901 (2012).
- [65] Samuel L. Braunstein and Peter van Loock, Quantum information with continuous variables, Rev. Mod. Phys. 77, 513-577 (2005).
- [66] S. Barzanjeh, S. Pirandola, D. Vitali, and J. M. Fink, Microwave quantum illumination using a digital receiver, Sci. Adv. 6, eabb0451 (2020).
- [67] S. Lloyd, Enhanced sensitivity of photodetection via quantum illumination, Science 321, 1463 (2008).